Topics in Catalysis
https://doi.org/10.1007/s11244-025-02051-w

ORIGINAL PAPER

AuPd/TiO_2 Catalysts in the CO Oxidation: Insights into the Synthesis Procedure and In-situ Spectroscopy Studies

Daniel G. Araiza[1] · Misael Fernández[1] · Mariana Sánchez-Ugalde[1] · Aida Miranda[2] · Dora A. Solís-Casados[3] · Viridiana Maturano-Rojas[1] · Rodolfo Zanella[1]

Accepted: 31 December 2024

Abstract
A series of bimetallic AuPd/TiO_2 catalysts (Au/Pd = 1) were prepared through either the impregnation or the deposition-precipitation in urea (DPU) approach and tested in the CO oxidation reaction. Among these, the sample synthesized through a sequential impregnation (Pd) followed by DPU (Au), with an intermediate thermal treatment in air, presented a remarkable CO conversion at sub-ambient temperatures and an enhanced catalytic stability, compared to the monometallic samples. The ex-situ characterization revealed that the synthesis procedure led to the formation of well-dispersed bimetallic AuPd nanoparticles over the TiO_2 support. The in-situ characterization helped to propose that bimetallic NPs were composed of an intermetallic Au-Pd phase with both atoms available in the surface. Both in-situ FTIR and UV-vis spectroscopies helped to recognize the active sites during the reaction: Au in close interaction with the TiO_2 at low temperatures, and step/edges Pd sites at high temperatures. Finally, the pivotal role of the TiO_2 reducibility in the CO oxidation reaction, promoted by the bimetallic AuPd NPs, was determined through in-situ Raman spectroscopy.

Keywords CO oxidation · Intermetallic Au-Pd NPs · TiO_2 reducibility · In-situ spectroscopy

1 Introduction

It is well-established that both gold (Au) and palladium (Pd)-based catalysts present good performances in the CO oxidation reaction, especially when a reducible oxide is employed as a support [1–3]. Au nanoparticles (NPs) have excelled mostly as part of the Au/TiO_2 system [1], where the particle size is crucial in the high catalytic activity [4]. Whereas the Pd NPs have proved their high efficiency in Pd/CeO_2 catalysts [2], and the close interaction between palladium and the Ce^{4+}/Ce^{3+} redox pair has been proposed to be responsible for the enhanced activity [5].

In this regard, some studies have shown the enhancement in the CO conversion of bimetallic AuPd nanoparticles (NPs) supported on TiO_2 [6–9]. Moreover, the methodology employed to prepare these supported AuPd NPs (including the thermal treatments) has impacted on their catalytic activity. For example, L. Guczi et al. observed a slight increase in the CO conversion for bimetallic AuPd/TiO_2 catalysts prepared by a sol-gel process compared to their monometallic counterparts [9]. However, the thermal treatment required to remove organic residues from the synthesis increased the particle size, thereby reducing their activity. L. Delannoy et al. prepared bimetallic AuPd/TiO_2 catalysts by a one-step deposition-precipitation with urea (DPU) method [6]. A better catalytic stability under CO oxidation conditions was reported in the bimetallic sample, nonetheless, the sample contained a high total amount of metal (9 wt%). More recently, G. Tofighi et al. explored a novel colloidal approach to prepare AuPd/TiO_2 catalysts using a microfluidic reactor setup [8]. Although the Pd-rich bimetallic

✉ Daniel G. Araiza
daniel.araiza@icat.unam.mx

✉ Rodolfo Zanella
rodolfo.zanella@icat.unam.mx

[1] Instituto de Ciencias Aplicadas y Tecnología, Universidad Nacional Autónoma de México, Circuito Exterior s/n, Ciudad Universitaria, Ciudad de México 04510, Mexico

[2] Instituto de Investigaciones en Materiales, Universidad Nacional Autónoma de México, Circuito Exterior s/n, Ciudad Universitaria, Ciudad de México 04510, Mexico

[3] Centro Conjunto de Investigación en Química Sustentable UAEM-UNAM, Carretera Toluca- Atlacomulco Km 14.5, Unidad San Cayetano, Toluca, Estado de México C.P. 50200, Mexico

Published online: 27 January 2025

sample surpassed the activity of the monometallic counterparts, the elevated costs of synthesis are worth-considered.

In all the above-mentioned works, both metals were added at the same time, regardless of the synthesis approach. However, another crucial parameter to consider when synthetizing supported bimetallic systems is the order in the addition of the metals: the adequate sequence will depend on the nature of the catalysts (NPs and support), as well as on the type of catalytic reaction under study. The above recognizes that the interaction of each metal with the surface of the support is different, and employing a specific synthesis methodology could enhance the interaction between the two metals, among other properties. For example, C. Betti et al. studied different $PtNi/Al_2O_3$ catalysts and found that the incipient wetness impregnation of platinum and nickel precursors (in that order) improved the selectivity in the catalytic hydrogenation of styrene [10]. On the other hand, in bimetallic $NiCo/Al_2O_3$ catalysts, the sequential wet impregnation of first nickel and then Co increased the catalytic activity of the Fischer-Tropsch (FT) synthesis [11].

Nonetheless, the use of different methodologies for the deposition of each metal in bimetallic Au-M/TiO_2 systems has been barely explored. One of the few is the work by G. Díaz et al. [12], where a combined DPU + incipient wetness impregnation method was used to prepare bimetallic IrAu/TiO_2 catalysts; this approach allowed an improved activity in the citral hydrogenation. Moreover, our research group has successfully explored the obtention of highly active bimetallic Au-M/TiO_2 catalysts (M = Ag, Ru and Rh) in the CO oxidation reaction, through the metal(s) addition by different approaches [13–15].

In this frame, the present investigation was focused on obtaining highly active bimetallic AuPd/TiO_2 catalysts for the CO oxidation reaction. For this purpose, two different methodologies, i.e., deposition-precipitation with urea (DPU) and impregnation, were explored thoroughly for the metal(s) addition. Besides, the addition sequence and intermediate thermal treatments were variables considered to generate the most active bimetallic catalyst.

Furthermore, to properly identify the active sites in the bimetallic AuPd/TiO_2 catalysts, in-situ spectroscopic techniques such as FTIR [16], UV-vis [17], and Raman [18], were implemented. The combination of the three techniques could reveal specific parts of the supported catalysts, like the surface arrangement of bimetallic NPs [19], the optical and plasmonic properties of NPs [20], and the structural feature of metal oxides employed as support [21].

2 Experimental

2.1 Synthesis of Catalysts

Monometallic Au and Pd NPs, synthesized through different routes, were deposited onto a commercial TiO_2 support (AEROXIDE® TiO_2 P25, $S_{BET} = 50 \pm 15$ m^2 g^{-1}). The nominal contents of gold and palladium were set at 3.0 wt% and 1.68 wt%, respectively, in order to achieve an Au: Pd atomic ratio of 1.0:1.0 in the bimetallic samples. Au NPs were added through the DPU method, widely described in previous works [13, 14, 22]. In this case, $HAuCl_4 \cdot 3H_2O$ (Aldrich Cat. No. 520918) and NH_2CONH_2 (Aldrich Cat. No. U5378) were used as reagents. For Pd NPs, two routes were explored: the aforementioned DPU and a traditional impregnation approach. In both cases, $Pd(NO_3)_2 \cdot H_2O$ (Aldrich Cat. No. 205761) was employed as the metal precursor. Bimetallic AuPd NPs deposited over the TiO_2 were synthetized by adding the metals sequentially: first palladium (DPU or impregnation) and then gold (DPU). After the addition of the metal(s), regardless of the methodology (DPU or impregnation), solids were dried under vacuum at 80 °C for 2 h. Besides, the use (or not) of a thermal treatment at 400 °C, between the addition of palladium and gold NPs was explored, with two different atmospheres (air and H_2). The variables explored during the synthesis procedure and the sample labeling of each catalyst are summarized in Table S1 of the Supplementary Information.

2.2 Characterization of Catalysts

The metallic composition was determined through EDS characterization. The analyses were performed with an Oxford AZtec microanalysis system coupled to a JEOL 5900-LV SEM microscope, operating at 20 kV. Measurements were taken across over thirty different zones. The elemental analyses were corroborated through X-ray fluorescence (XRF), employing a XEPOS HE (AMETEK) spectrometer. The structure was studied through X-ray diffraction (XRD). Patterns were obtained in a Siemens Diffractometer (D5000), using CuKα radiation (λ = 1.5425 Å) and data collection at the 2θ = 20–80° interval, each 0.03° s^{-1}. The GSAS-II software was employed in the Rietveld refinement [23]. Raman spectroscopy was employed to complement the structural features. Spectra were collected in a WITec alpha300 RA spectrometer, with a 532 nm laser and 3.56 mW. Data were obtained with 0.2 s of integration time and 50 accumulations. The reducibility was studied via H_2-TPR experiments, performed in a Micromeritics Analyzer (AutoChem II 2920) coupled to a TCD detector. For the analysis, a 10%H_2/Ar gas flow (25 mL min^{-1}) was submitted to the dried sample (~0.050 g) while increasing the temperature (10 °C min^{-1}),

from − 20 °C up to 600 °C. The particle size of the metal NPs was obtained through TEM characterization. The study was carried out in a JEM 2010 F FasTem microscope, equipped with a Z-contrast annular (HAADF) detector and operating at 200 kV. Finally, characterization through XPS was achieved using a JEOL JPS 9200 XPS apparatus. Data were collected with a 20 kV pass energy, 300 W and 20 scans, and employing Al Kα X-ray radiation (1486.6 eV). The C*1s* signal at 284.8 eV was employed to adjust the charge.

2.3 Catalytic Tests in the CO Oxidation Reaction

The CO oxidation reaction was evaluated in a continuous-flow fixed-bed reactor coupled to an Agilent 7820 A gas chromatograph (FID detector and a CP-Sil 5 CB capillary column). The sample (0.040 g) was in-situ activated in a H_2 atmosphere (40 mL min^{-1}) at 500 °C (2 °C min^{-1}) for 2 h. The reaction started when the reactive mixture (1 vol% of CO, 1 vol% of O_2, N_2balanced) flowed in the reactor at a 100 mL min^{-1} rate, while increasing the temperature from − 5 °C up to 300 °C (2 °C min^{-1}). Additionally, stability tests were performed at 50 °C during a 24 h run. In this case, after the activation step, samples were heated in N_2atmosphere at a 2 °C min^{-1}rate to reach the target temperature (50 °C). All catalytic tests were carried out over samples diluted through mechanical mixing (20 wt% of sample, 80 wt% of bare TiO_2 support). The dilution was carried out due to high activity presented by the undiluted samples, even at sub-ambient temperatures (data not shown).

2.4 In-situ Characterization Through Spectroscopic Techniques

Three in-situ spectroscopic techniques (FTIR, UV-vis and Raman) were implemented separately, to determine the active sites and monitor the possible structure modifications of catalysts when interacting with different reactive atmospheres (H_2 and $CO+O_2$). Prior to all analyses, samples were in-situ activated using the same conditions (H_2, 500 °C). The CO oxidation tests were conducted under conditions similar to those described in Sect. 2.3.

Diffuse reflectance FTIR analyses were conducted in a temperature-controlled DRIFT cell (Harrick) coupled to a Thermo Scientific Nicolet iS50 spectrometer, collecting data at a 4 cm^{-1} of resolution, each 128 scans. After activation, the sample (ca. 0.050 g.) was cooled down to −20 °C under flowing N_2, while recording data each 50 °C. The reported spectra considered the subtraction before and after the activated sample interacted with the reactive atmosphere. Diffuse reflectance UV-vis absorption characterization was carried out in an Agilent CARY 5000 spectrophotometer, coupled to a temperature-controlled reaction cell (Harrick). Data were recorded at the 300–800 nm interval, considering the subtraction of the background spectrum recorded with Teflon. The sample (ca. 0.050 g) was in-situ activated while collecting absorption spectra. Raman spectroscopy measurements were collected in a Princeton TriVista 557 coupled to an Olympus BX51 microscope (100x objective magnification) and a Nd: YVO_4 laser (532 nm). The sample (ca. 0.10 g) was converted into pressed pellets and deposited inside a temperature-controlled reaction cell (Linkam THMS600). Spectra were collected at the 150–800 cm^{-1} interval, with a 1.9 cm^{-1} of resolution, and data acquisition of 25 s for 25 times.

3 Results and Discussion

3.1 Effect of the Synthesis Procedure of Bimetallic AuPd/TiO_2 Catalysts in the CO Oxidation

3.1.1 Activity Tests

Table S1 of the SI summarizes the different methodologies employed in the synthesis of the catalysts. In all cases, the addition of gold was done through the DPU approach; this route has resulted in the obtention of deposited Au NPs with small sizes and narrow particle size distribution [13, 14]. Besides, in previous works related to bimetallic Au-M/TiO_2 catalysts employed in the CO oxidation reaction (where M has been Cu, Ag or Rh), improved catalytic properties have been found when Au NPs were added secondly, after the first M metal [13, 14, 22]. Therefore, in the present work, the variables explored in the synthesis procedure of bimetallic samples were the following: (i) the addition method of the palladium precursor, and (ii) the intermediate thermal treatment between the addition of the palladium and gold NPs. Prior to the catalytic tests, dried samples were in-situ activated in an H_2 atmosphere at 500 °C. The activation temperature was selected based on the highest CO conversion exhibited by a bimetallic AuPd/TiO_2 control sample thermally treated at different temperatures: 300, 400, 500 and 600 °C (see Table S2 of the SI). The activation temperature range was selected based on the H_2-TPR characterization, ensuring the complete reduction of the Au and Pd species (this is discussed in detail in Sect. 3.2.2**).**

The catalytic activity results of the diluted bimetallic AuPd/TiO_2 catalysts, prepared through different approaches, are presented in Fig. 1. For comparison purposes, the results of the monometallic samples are included in all graphs. First, the activity profile of the gold sample presented around 15% of conversion at 0 °C, then, the conversion abruptly increased up to 75% in the 0–30 °C interval, and finally it gradually increased until it reached

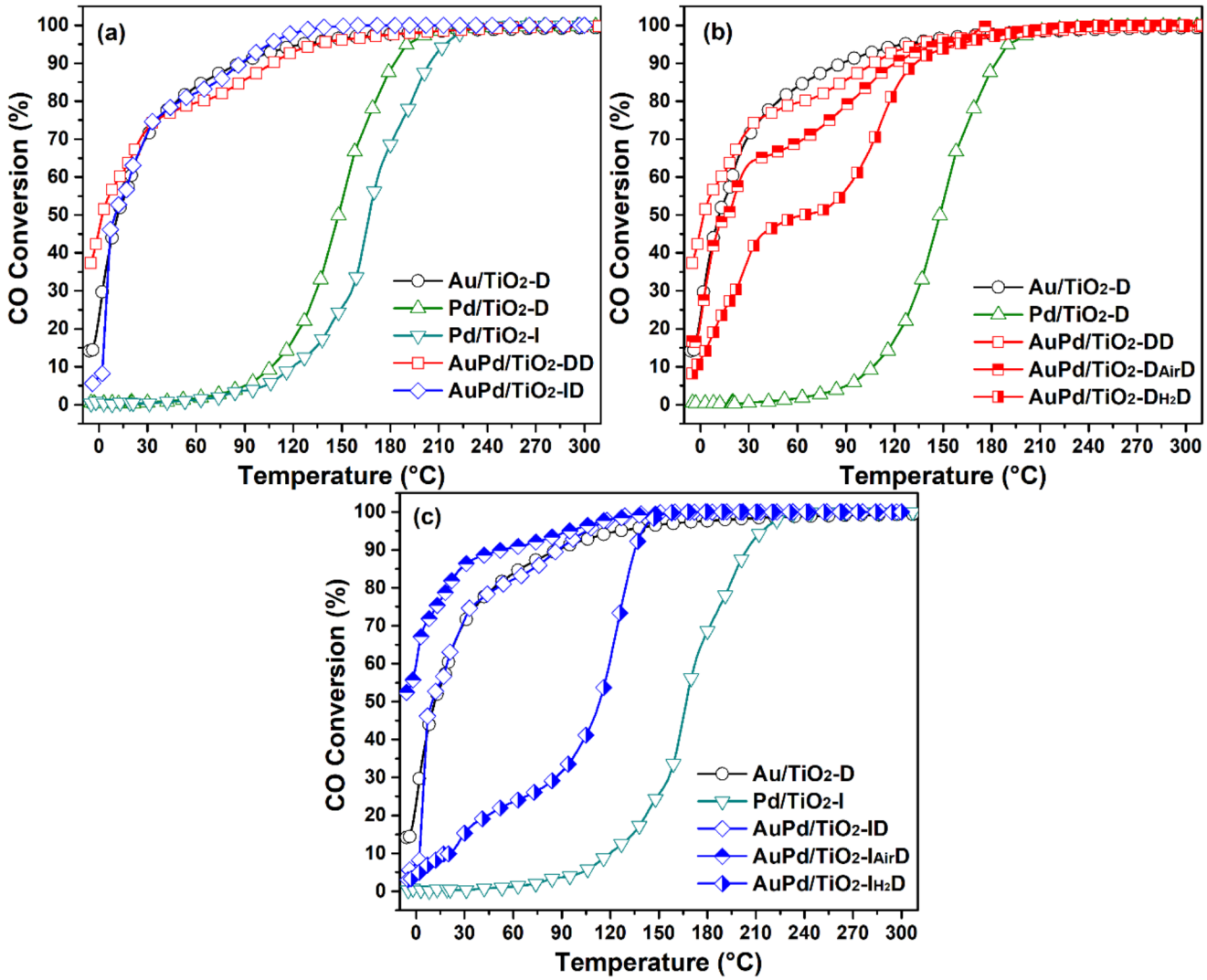

Fig. 1 CO conversion (%) as a function of the reaction temperature (− 5 to 300 °C) of diluted mono and bimetallic catalysts prepared through different approaches: (**a**) without an intermediate thermal treatment, (**b**) sequential DPU-DPU with an intermediate thermal treatment, (**c**) sequential Imp.-DPU with an intermediate thermal treatment

total conversion at around 200 °C. On the other hand, palladium samples showed a typical "S-shaped" curve, with a light-off temperature at ca. 120 °C, and total conversion above 210 °C. In summary, results indicated that among the two metals, gold NPs supported on TiO_2 were more active for the CO oxidation reaction, especially at sub-ambient temperatures, with the following trend: Au/TiO_2-D>>Pd/TiO_2-D>Pd/TiO_2-I.

In the first set of bimetallic samples, Fig. 1a, two routes of depositing the Pd NPs, without intermediate thermal treatments, were explored: impregnation (AuPd/TiO_2-ID) and DPU (AuPd/TiO_2-DD). Activity results showed that the AuPd/TiO_2-DD catalyst exhibited a higher activity only at temperatures below 0 °C, 35%, compared to the 15% observed in the gold counterpart. However, right after this temperature, bimetallic catalysts prepared without an intermediate thermal treatment presented an activity profile almost similar to the monometallic Au/TiO_2-D sample. This slightly improved activity suggests the formation of bimetallic AuPd entities, as both metals are miscible and prone to form intermetallic alloys [24]. Nevertheless, this interaction became less important with the temperature, suggesting the absence of an important synergism between gold and palladium. In view of the above, other variables during the preparation were explored.

In the second set of bimetallic samples, Fig. 1b, the samples were thermally treated in either an oxidative (air) or reductive (H_2) atmosphere, between the Pd and the Au deposition on the TiO_2 support (both through the DPU approach). Results showed that, regardless of the atmosphere, the intermediate thermal treatment did not improve the CO conversion of the bimetallic samples, compared to

the performance of the monometallic gold catalyst. Moreover, the sample without an intermediate thermal treatment (AuPd/TiO_2-DD) also presented a better activity behavior than their counterparts, suggesting that the thermal process affected some key catalytic features of the supported bimetallic AuPd NPs. Interestingly, among the two samples, the one treated in air showed a better performance (AuPd/TiO_2-$D_{Air}D$), indicating that the atmosphere affected the stabilization of the Pd NPs and their interaction with gold.

In the third set of bimetallic samples, the intermediate thermal treatment was included after the impregnation of the Pd NPs, either in an oxidative (AuPd/TiO_2-$I_{Air}D$) or a reductive (AuPd/TiO_2-$I_{H2}D$) atmosphere. Surprisingly, only the bimetallic AuPd/TiO_2-$I_{Air}D$ catalyst presented an improved activity in all the temperature range, compared to the one exhibited by the monometallic gold sample. Right from the beginning (−5 °C), the bimetallic catalyst presented a 50% conversion, almost five times larger than that observed in the Au/TiO_2-D catalyst. Afterwards, the activity rapidly increased up to 85% in the 0–30 °C interval, followed by a gradual increase until total conversion, observed at ca. 150 °C. On the other hand, the CO conversion exhibited by the AuPd/TiO_2-$I_{H2}D$ catalyst decreased considerably (as in the case of the AuPd/TiO_2-$D_{H2}D$ sample), and the activity profile resembled that from the monometallic Pd/TiO_2-I sample.

3.1.2 Metal Content and TEM Characterization

The metal content, determined *via* EDS measurements (and corroborated through XRF analyses), as well as the TEM characterization, were implemented, as a first approach, to evaluate the effectiveness of the different methodologies for synthesizing bimetallic AuPd NPs (summarized in Table S1) and to correlate those features with the catalytic activity of the samples. Table 1 provides the results concerning the amount of metal deposited (wt%) obtained from EDS measurements of the dried samples. As expected, the experimental amount of gold deposited through the DPU approach was very close to the nominal value (3.0 wt%).

Conversely, the experimental amount of palladium deposited over the TiO_2 depended on the procedure of preparation. When DPU route was employed, the amount of palladium (~0.4 wt%) was only 25% of the nominal one (1.62 wt%); however, through the impregnation route, the value increased significantly (~1.3 wt%), almost 80% of the expected value. Results clearly indicated that the DPU procedure is not effective for the deposition of Pd NPs over the TiO_2 surface, at least under the experimental conditions described in Sect. 2.1. This could be one of the main reasons why bimetallic catalysts prepared through a sequential Pd and Au deposition (both through the DPU approach) were not as effective in the CO oxidation (see Fig. 1a, b). On the other hand, the Au:Pd atomic ratio of samples where the palladium precursor was added through the impregnation method was almost the expected (i.e., 1).

Table 1 also summarizes the mean particle size (nm) from the activated catalysts. Measurements were conducted from the identified NPs (bright spots) obtained through the TEM-HAADF characterization. All the representative TEM images are presented in Fig. S1 of the SI, including the particle size histograms. TEM images of the most active bimetallic catalyst, alongside its counterparts, are also shown in Sect. 3.2.3. The bright spots were linked to the metallic NPs, either gold or palladium. Focusing on the monometallic samples, the synthesis procedure affected the size of the Pd NPs, which were smaller in the Pd/TiO_2-D catalyst (2.6 nm), and this catalyst also showed a slightly better catalytic activity (see Fig. 1a). On the other hand, bimetallic samples prepared through a sequential DPU Pd and Au deposition, with an intermediate thermal treatment, exhibited mean particle size values near to the one from the monometallic Au/TiO_2-D catalyst (3.7 nm). Therefore, the unimproved catalytic activity exhibited by these samples (see Fig. 1b) was not associated with the size of the particles, but probably to lower Pd content (~0.4 wt%). Finally, the mean particle size of the bimetallic samples prepared through a sequential impregnation (Pd) and DPU (Au) approach presented the following tendency: AuPd/TiO_2-ID (4.0 nm)<AuPd/TiO_2-$I_{H2}D$ (4.4 nm)<AuPd/TiO_2-$I_{Air}D$ (4.9 nm). Overall, the NPs were well-dispersed, and their values fell between those of the monometallic counterparts (3.7 nm for gold and 5.4 nm for palladium). After the intermediate thermal treatment in

Table 1 Metal content (wt%), bimetallic atomic ratio (Au:Pd), and mean particle size (nm) of Au/TiO_2, Pd/TiO_2 and bimetallic AuPd/TiO_2 catalysts synthesized through different approaches

Sample	Metal content (wt%)[a]		Au: Pd atomic ratio[a]	Mean particle size (nm)[b]	
	Au	Pd		Activated[c]	Spent[d]
Au/TiO_2-D	2.8	n/a	n/a	3.7 (0.8)	3.9 (1.0)
Pd/TiO_2-D	n/a	0.4	n/a	2.6 (0.6)	n/a
Pd/TiO_2-I	n/a	1.4	n/a	5.4 (1.4)	n/a
AuPd/TiO_2-DD	2.6	0.5	1.0:0.3	3.0 (1.1)	n/a
AuPd/TiO_2-$D_{Air}D$				3.6 (0.8)	n/a
AuPd/TiO_2-$D_{H2}D$				3.7 (0.8)	n/a
AuPd/TiO_2-ID	2.4	1.2	1.0:0.9	4.0 (0.9)	n/a
AuPd/TiO_2-$I_{Air}D$				4.9 (1.2)	4.8 (2.0)
AuPd/TiO_2-$I_{H2}D$				4.4 (2.1)	n/a

[a]Determined from EDS measurements of fresh samples.

[b]Determined fromTEM measurements of activated samples; standard deviation (SD) in parenthesis.

[c]Samples activated at 500 °C in the H_2 atmosphere for 2 h.

[d]Samples recovered after the stability tests (50 °C, 24 h)

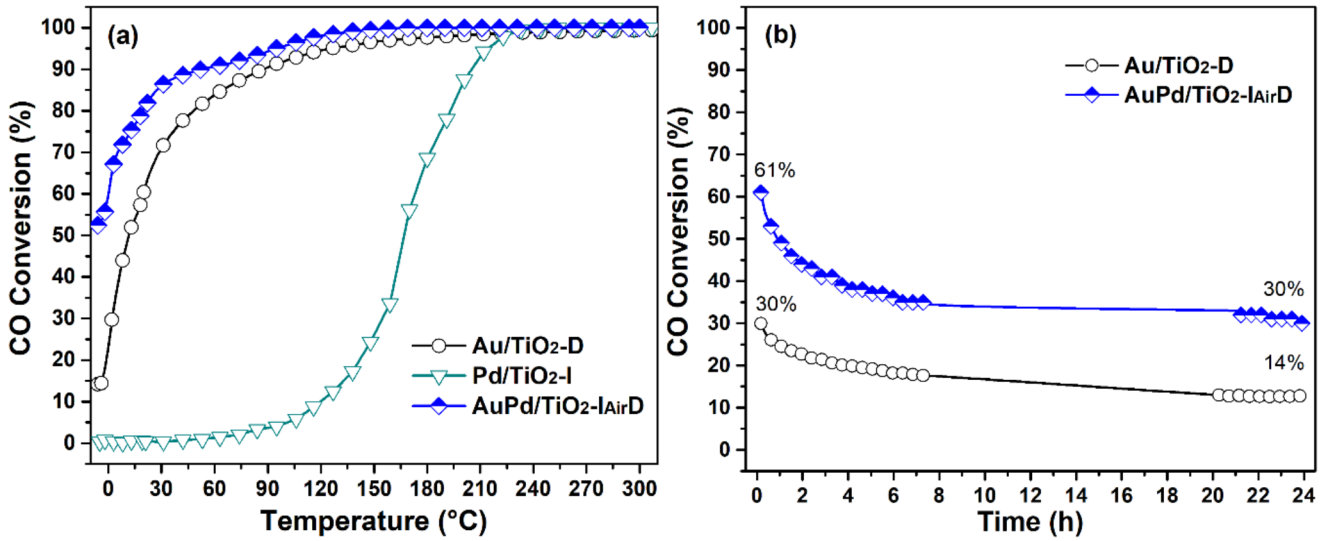

Fig. 2 (**a**) CO conversion (%) as a function of the reaction temperature (− 5–300 °C) of the most active bimetallic catalyst: sample prepared by sequential Impregnation (Pd)– DPU (Au) with an intermediate thermal treatment (air, 400 °C). (**b**) CO conversion (%) as a function of the reaction time (24 h) at 50 °C

Table 2 Metal dispersion (%), catalytic properties and kinetic data of Au/TiO_2-D, Pd/TiO_2-I and $AuPd/TiO_2$-I_{Air}D catalysts

Sample	Metal dispersion (%)[a]	Contact time (g_{cat} h mol^{-1}_{CO})	Reaction rate (mol_{CO} mol^{-1}_{Metal} s^{-1})		TOF (s^{-1})		E_a (kJ mol^{-1})
			0 °C	10 °C	0 °C	10 °C	
Au/TiO_2-D	32	3.2	0.172	0.301	0.532	0.931	30
Pd/TiO_2-I	21		0.002	0.003	0.010	0.014	n/a
$AuPd/TiO_2$-I_{Air}D	24		0.191	0.214	0.807	0.906	16

[a]Metal dispersion was calculated employing the mean particle size values from the TEM observations, assuming a spherical model.

air, the mean particle size slightly increased. Nonetheless, the $AuPd/TiO_2$-I_{Air}D catalyst presented the best activity (see Fig. 1c). Therefore, the enhanced catalytic performance exhibited by this sample should be not only ascribed to a particle size effect, but also to a specific Au-Pd interaction and surface arrangement obtained through this synthesis procedure.

In this frame, two considerations are worth mentioning. First, after the intermediate treatment with H_2, an increased amount of Pd^0 species is expected, whereas after the intermediate treatment with air, PdO_X species are probably more abundant. Second, the activity results for the bimetallic catalysts showed that, when a reductive atmosphere was employed in the intermediate treatment, a decrease in the CO conversion was noticed, regardless of the addition method of the palladium (Fig. 1b, c). Based on these two observations, it is proposed that the interplay between Pd^0 and the gold precursor species (Au^{3+}) led to the formation of bimetallic AuPd entities with less synergy, Conversely, the PdO_X-Au^{3+} interaction resulted in bimetallic AuPd NPs with a higher synergy, especially when Pd was added via impregnation ($AuPd/TiO_2$-I_{Air}D), improving the catalytic properties.

3.1.3 Catalytic Properties of the Bimetallic $AuPd/TiO_2$ Samples

The profile of the most active bimetallic catalyst ($AuPd/TiO_2$-I_{Air}D) and its monometallic counterparts (Au/TiO_2-D and Pd/TiO_2-I) are presented separately in Fig. 2a. By taking a closer look at these results, although the CO conversion was higher in the $AuPd/TiO_2$-I_{Air}D sample, especially from − 5 °C to 30 °C, the activity profile resembled the one observed in the monometallic Au/TiO_2-D sample. Therefore, the apparent activation energies (E_a) of both catalysts were calculated (see Arrhenius plots in Fig. S2) and the data results are presented in Table 2. The $E_a$value of the bimetallic $AuPd/TiO_2$-I_{Air}D catalyst (16 kJ mol^{-1}) was approximately half that of the monometallic gold counterpart (30 kJ mol^{-1}). This suggests an enhancement in the reactivity of the Au sites, likely due to their close interaction with the Pd atoms. Similar behavior has been reported for bimetallic Au-Cu and Au-Rh NPs supported on $TiO_2$and tested in CO oxidation reaction [14, 22]. Table 2also presents the reaction rates and TOF data obtained under kinetic regime. At 0 °C, the TOF value for the $AuPd/TiO_2$-I_{Air}D sample (0.807 s^{-1}) was nearly double that of the Au/TiO_2-D catalyst (0.532 s^{-1}),

providing clear evidence of the enhanced catalytic activity of the bimetallic sample. At 10 °C, both TOF values were similar, indicating that the beneficial role of Pd in the bimetallic sample was more relevant at low temperatures.

Furthermore, the catalytic stability of the most active samples in this series (AuPd/TiO_2-I_{Air}D and Au/TiO_2-D) was studied at 50 °C for 24 h, and results are presented in Fig. 2b. At the beginning of the run, the bimetallic AuPd/TiO_2-I_{Air}D sample exhibited the highest activity (61%), followed by the monometallic Au/TiO_2-D (30%). After 4 h on stream, a significant drop in the CO conversion was observed in the AuPd/TiO_2-I_{Air}D catalyst (40%). From this stage, the bimetallic sample presented only slight deactivation, and, at the end of the experiment, the CO conversion was around 30%. On the other hand, the monometallic sample presented a continuous drop in the activity during the 24 h of run, and exhibited final CO conversion values near 13%. At the end of the test, the deactivation percentage values were the following: Au/TiO_2-D (57%) and AuPd/TiO_2-I_{Air}D (50%). This result indicated that the presence of palladium in the bimetallic AuPd/TiO_2-I_{Air}D catalyst not only enhanced the activity, but also the stability of the sample. TEM-HAADF characterization of the spent samples (50 °C, 24 h) was useful to propose an explanation for the enhanced stability (see Table 1): while the particle size slightly increased in the monometallic Au/TiO_2-D sample (3.9 nm), it remained nearly unchanged in the bimetallic AuPd/TiO_2-I_{Air}D catalyst (4.8 nm).

In the following sections, these three catalysts (Au/TiO_2-D, Pd/TiO_2-I and AuPd/TiO_2-I_{Air}D) were studied in detail to unveil the key structural features that led into their effectiveness in the CO oxidation reaction.

3.2 Ex-situ Characterization of Catalysts

3.2.1 Structural Characterization by XRD and Raman Spectroscopy

Figure 3a presents the XRD patterns of three samples (Au/TiO_2-D, Pd/TiO_2-I and AuPd/TiO_2-I_{Air}D) at different stages: dried, activated (500 °C, H_2) and spent (deactivation tests). In all cases, the characteristic diffraction peaks of both TiO_2 anatase (JCPDS 021–1272) and TiO_2 rutile (JCPDS 021–1276) were identified. These signals originated from the commercial TiO_2 support (AEROXIDE® TiO_2 P25). Figure 3b shows that, after activation, TiO_2 (101) diffraction peaks from gold-containing catalysts shifted to lower angles (i.e., lattice expansion), while the opposite occurred in the samples spent (i.e., lattice contraction). Rietveld refinement of all the XRD patterns was carried out to confirm the above and the complete results are presented in Table S2. A summary of the values of the "a" parameter of the TiO_2 anatase phase is included in Table 3. The TiO_2 lattice expansion could be related to the partial reduction of the support upon activation in hydrogen, as the ionic radius of Ti^{3+} (0.67 Å) is larger than that of Ti^{4+} (0.61 Å) [25, 26]. On the other hand, TiO_2 lattice contraction revealed some restructuring of the catalysts after the deactivation tests.

Figure 3c presents an 2θ amplification where the main signals of the metal NPs (Au and Pd/PdO) reside. No diffraction peaks related to gold or palladium-based phases were observed in any case (dried, activated or spent samples). These results suggested that the metal NPs were well-dispersed over the TiO_2 surface (activated catalysts) but also that after the stability tests, these NPs did not significantly increase. The above agreed with the mean particle size values of the spent samples (Table 1).

The structural features of the catalysts (dried, activated and spent) were complemented through Raman spectroscopy, Fig. 4a. All normalized spectra exhibited the characteristics Raman signals of the TiO_2 anatase phase, located at 144 cm^{-1} ($E_{g(1)}$), 197 cm^{-1} ($E_{g(2)}$), 397 cm^{-1} ($B_{1g(1)}$), 516 cm^{-1} ($A_{1g}+B_{1g(2)}$), and 638 cm^{-1} ($E_{g(3)}$) [27]. Most of the TiO_2 rutile active modes reside at around the same Raman shifts, and these contributions were probably overshadowed. The most intense Raman active mode of the anatase phase, namely $E_{g(1)}$, accounts for the symmetrical stretching vibrations of the O-Ti-O groups, and it is sensitive to the presence of oxygen vacancies (Vö) [28, 29]. Furthermore, it has been well-established that the $E_{g(1)}$ mode displacement towards higher Raman shifts indicates an increase of the Vö sites and, consequently, of the Ti^{3+} cations in the TiO_2 structure [30, 31].

Figure 4b presents an amplification of the spectra where the $E_{g(1)}$ was centered, and the displacements were clearly observed, depending on the reactive atmosphere. Compared to the dried samples, the activated ones presented the blue shift associated with the presence of Vö sites, and this phenomenon was more important in the AuPd/TiO_2-I_{Air}D catalyst, which indicated that the partial TiO_2 reduction was more important in this catalyst. Conversely, spent catalysts behaved differently; the $E_{g(1)}$ mode in both Au/TiO_2-D and Pd/TiO_2-I samples returned to its original position, while in the AuPd/TiO_2-I_{Air}D sample, the $E_{g(1)}$ blue shift increased (see Table 3). The above indicates that the reactive atmosphere ($CO+O_2$) affected the TiO_2 support differently in each catalyst; re-oxidation is suggested in both monometallic samples, while a further reduction probably occurred in the bimetallic one. This behavior could explain the differences in the activity and stability between the samples (see Fig. 2).

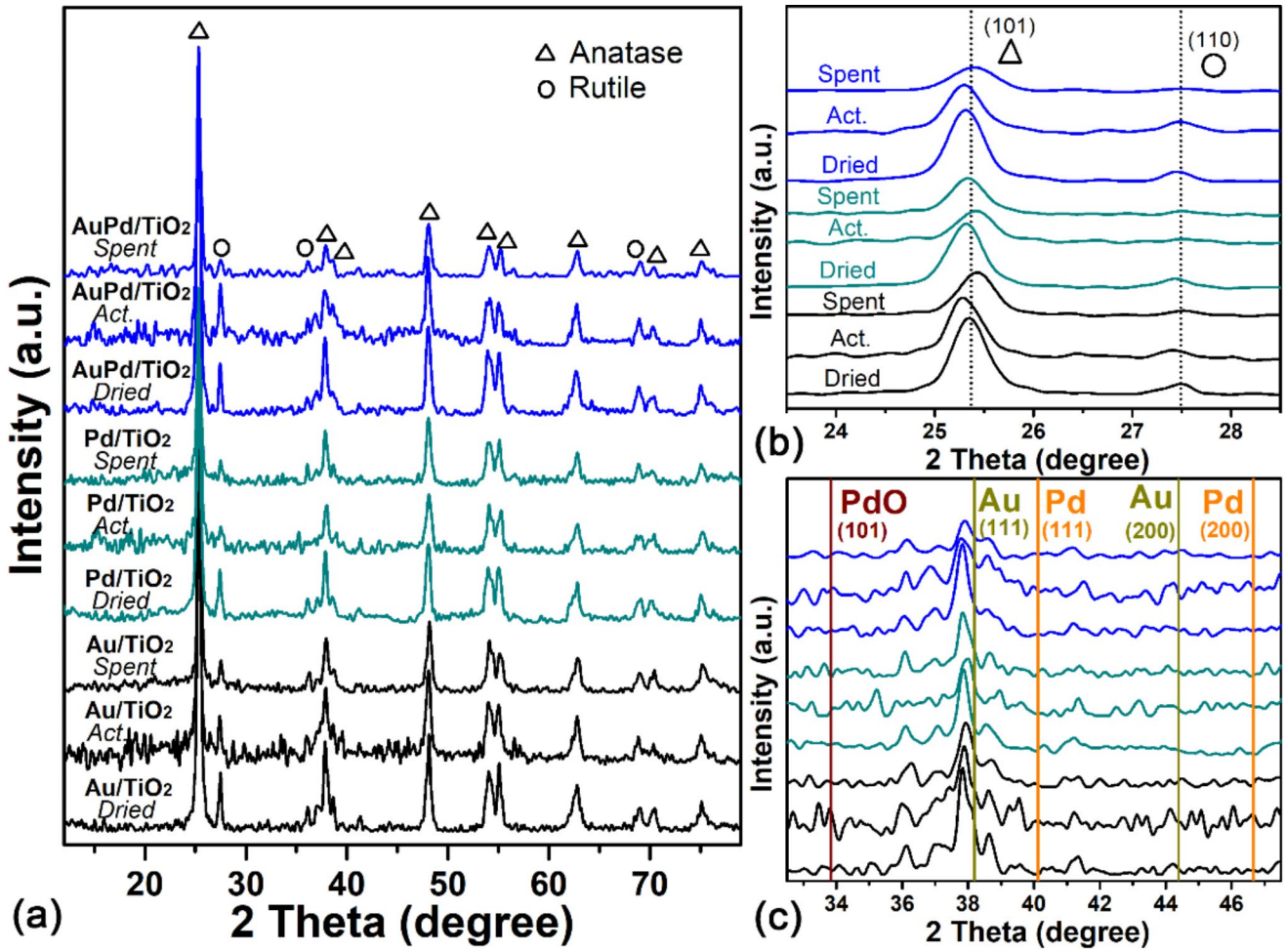

Fig. 3 (**a**) XRD patterns of dried, activated and spent catalysts. (**b**) The 2θ = 33 − 29° corresponds to the amplified zone, where the principal TiO_2 diffraction peaks reside, and (**c**) the 2θ = 32–48° corresponds to the amplified zone where the principal diffraction peaks of each metal (or metal oxide) reside

Table 3 Structural features (XRD, Raman), H_2 uptake (μmol) and optical properties (LSPR band) of Au/TiO_2-D, Pd/TiO_2-I and $AuPd/TiO_2$-I_{Air}D catalysts

Sample	Anatase "a" parameter (Å)			$Eg_{(1)}$ Raman mode (cm^{-1})			H_2 uptake (μmol)		LSPR band (nm)
	Dried	Act.[a]	Spent[b]	Dried	Act.[a]	Spent[b]	Exp.[c]	Theo.[d]	
Au/TiO_2-D	3.781	3.786	3.781	146.6	152.5	143.9	11.6	7.2	550
Pd/TiO_2-I	3.785	3.785	3.785	143.9	150.0	143.9	5.0	5.5	563, 628
$AuPd/TiO_2$-I_{Air}D	3.784	3.785	3.783	143.9	150.0	153.0	27.0	14.9	552, 621

[a]Samples activated at 500 °C in the H_2 atmosphere for 2 h

[b]Samples recovered after the stability tests (50 °C, 24 h)

[c]Determined from the H_2-TPR profiles of dried samples

[d]Calculated assuming stoichiometric reduction of Au^{3+} or Pd^{2+} species, as detected by EDS

3.2.2 Reducibility of Catalysts by H_2-TPR Experiments

The reducibility of dried samples was studied through H_2-TPR experiments performed from − 20 °C to 600 °C, Fig. 5. The profile of the Au/TiO_2-D sample revealed a single H_2 consumption event centered at 135 °C, with a small shoulder at around 150 °C. According to the literature, these contributions are related to the reduction of gold species interacting closely with the TiO_2 support, i.e., $Au^{3+} \rightarrow Au^0$ and $Au^{1+} \rightarrow Au^0$, respectively [32, 33]. The Pd/TiO_2-I sample exhibited a negative peak at 63 °C, attributed to the H_2 desorption from the decomposition of the palladium hydride phase after the reduction of palladium oxide species (i.e., PdO → PdH → Pd) [19]. The reduction of PdO

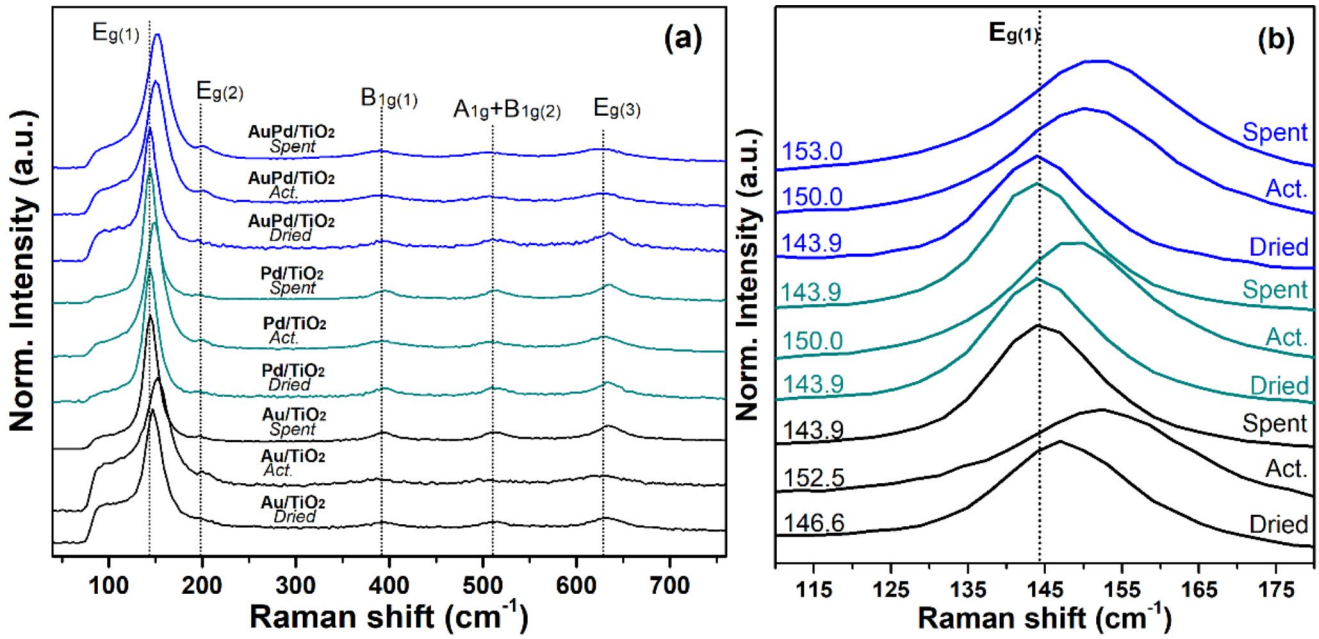

Fig. 4 (**a**) Normalized Raman spectra of dried, activated and spent catalysts. (**b**) The amplified zone where the principal TiO_2 anatase Raman peak ($Eg_{(1)}$) is located

species in PdO/TiO_2 samples has been reported to occur below 0°C [34]. Although experiments were carried out from sub-ambient temperature (−20 °C), the H_2 consumption associated with the reduction of oxidized palladium species was not observed. This result suggested that the process occurred spontaneously, without being recorded by the equipment. The Pd/TiO_2-I catalyst presented a second tiny contribution at ca. 290 °C, probably related to the reduction of PdOx species strongly interacting with the TiO_2 support.

Finally, the bimetallic $AuPd/TiO_2$-I_{Air}D sample presents a main H_2 consumption event at sub-ambient temperatures, with the maximum located at 17 °C. The absence of the reduction event at ca. 135 °C, observed in the monometallic Au/TiO_2-D sample, suggested that the 17 °C contribution originates from the reduction of gold species ($Au^{3+} \rightarrow Au^0$), and promoted by the presence of palladium; similar results have been reported in $AuPd/Al_2O_3$ catalyst [35]. Besides, the negative peak at 63 °C, associated with the H_2 desorption from Pd sites, indicated that the sub-ambient contribution also accounts for the reduction of palladium species. In summary, the H_2-TPR profile of the $AuPd/TiO_2$-I_{Air}D sample presented significant differences compared to its monometallic counterparts, and showed that both Au and Pd species were interacting closely, strongly suggesting the formation of an Au-Pd alloy [36].

The quantitative analysis of the H_2-TPR profiles is included in Table 3. The monometallic Pd/TiO_2-I sample presented a H_2 consumption close to the theoretical. Conversely, the experimental H_2 uptake from both gold-containing catalysts surpassed the expected one, more importantly in the bimetallic $AuPd/TiO_2$-I_{Air}D sample. The absence of contributions at higher temperatures (see inset Fig. 5), suggested that this increased H_2 uptake originates from the partial reduction of the TiO_2 support, promoted by the combined presence of Au and Pd species in the formed NPs.

3.2.3 Phase Identification of the NPs by HRTEM and XPS

As mentioned in Sect. 3.1, the most active bimetallic catalyst and its monometallic counterparts presented the following mean particle sizes: Au/TiO_2-D (3.7 nm), Pd/TiO_2-I (5.4 nm) and $AuPd/TiO_2$-I_{Air}D (4.9 nm).

To identify the crystalline phase of these NPs, activated catalysts were studied through high-resolution TEM, and the representative images are shown in Fig. 6. The identified NP from the Au/TiO_2-D catalyst (Fig. 6b) presented lattice fringe spacings of 0.246 and 0.248 nm, both related to (111) crystal planes of the metallic Au phase (JCPDS 04–0784). For the Pd/TiO_2-I catalyst (Fig. 6d), the observed NP exhibited lattice fringe spacing of 0.237 nm, associated with the (111) crystal planes of the metallic Pd phase (JCPDS 46–1043). Finally, the NP highlighted in the bimetallic $AuPd/TiO_2$-I_{Air}D sample showed lattice fringe spacing of 0.248, 0.244 and 0.213 nm (Fig. 6f). At first sight, these measures could be associated with two planes (111) and one plane (200) of metallic gold. However, since the values of the lattice from both Au and Pd metallic structures are very close, the formation of an Au-Pd alloy phase in the NPs was not discarded. The assumption where the NPs coming from the bimetallic $AuPd/TiO_2$-I_{Air}D catalyst were composed of

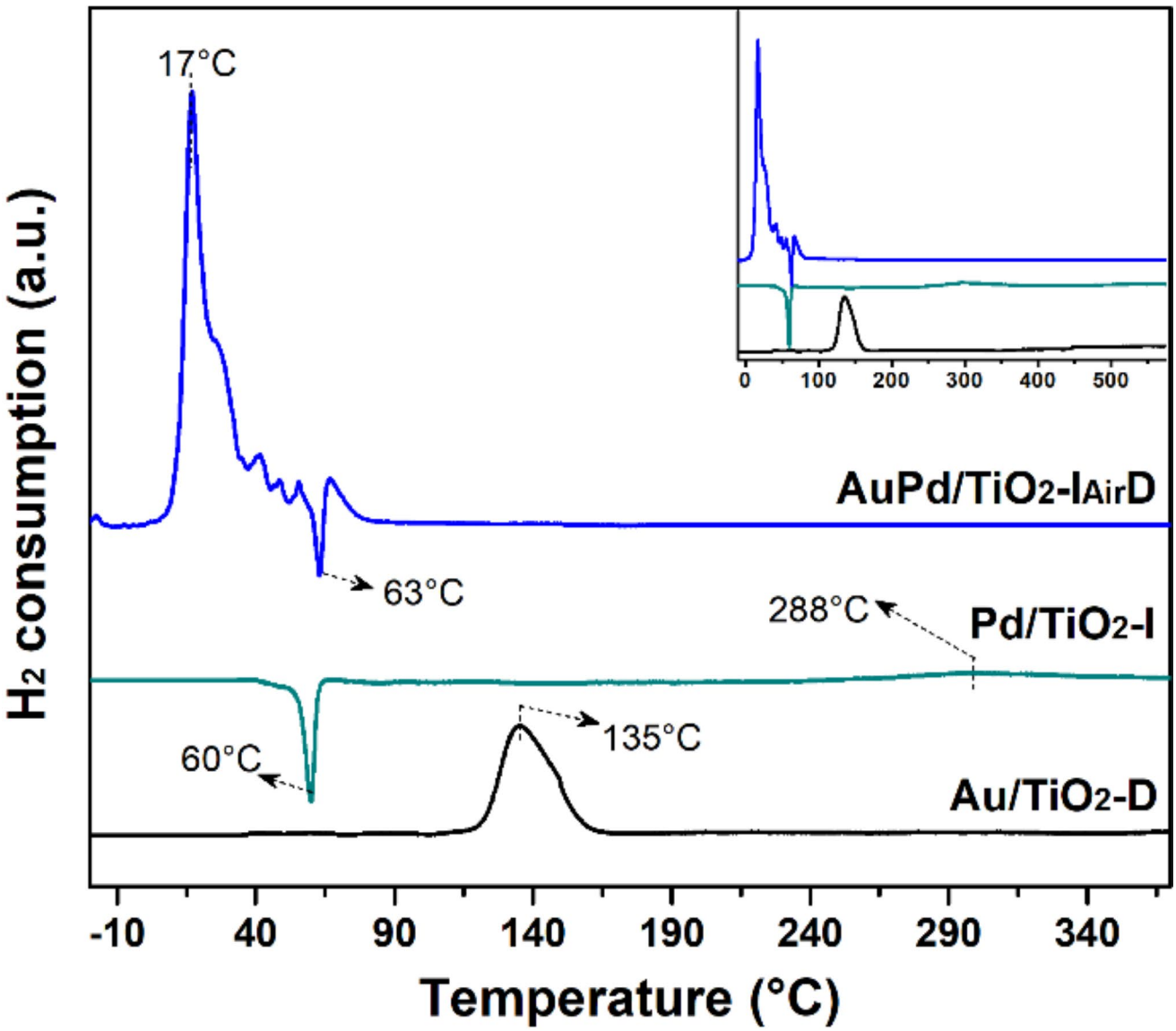

Fig. 5 H_2-TPR profiles of dried catalysts: Au/TiO_2-D, Pd/TiO_2-I and AuPd/TiO_2-I_{Air}D. Experiments were performed from −20 to 600 °C

an AuPd mixed phase (intermetallic or core-shell nanoparticles) could be strengthened by the single reduction event observed in H_2-TPR profile (see Fig. 5), which evidenced close interaction between Au and Pd species. Moreover, both Au and Pd present high miscibility and several reports have elucidated the formation of alloyed AuPd NPs [6, 8].

XPS characterization was implemented to corroborate the electronic state of gold atoms as well as the chemical environment of the Ti cations. Figure 7 shows the corresponding XPS spectra of the activated catalysts. The Au 4*f* edge deconvolution of both Au/TiO_2-D and AuPd/TiO_2-I_{Air}D samples is presented in Fig. 7a, b, respectively. In both cases, the presence of metallic Au NPs was corroborated with the contributions at around 81 eV (Au $4f_{7/2}$) and 85 eV (Au $4f_{5/2}$) [37]. The second doublet at lower binding energies, identified in both samples, may be related to the Au^0 species interacting closely with the Ti atoms from the support. Besides, no contributions at higher binding energies were observed (ca. 87 eV), which corroborated the absence of oxidized gold species in the gold-containing catalysts. Two important differences were identified in the bimetallic AuPd/TiO_2-I_{Air}D catalyst: (i) all contributions appeared shifted to lower binding energies, and (ii) the presence of a third doublet at ca. 78 and 82 eV. These features indicate modifications in the chemical environment of the Au^0 species, likely due to charge transfer from the bonded Pd^0 species. The above helped to strengthen the proposal for the formation of an AuPd alloy, in agreement with the HRTEM results.

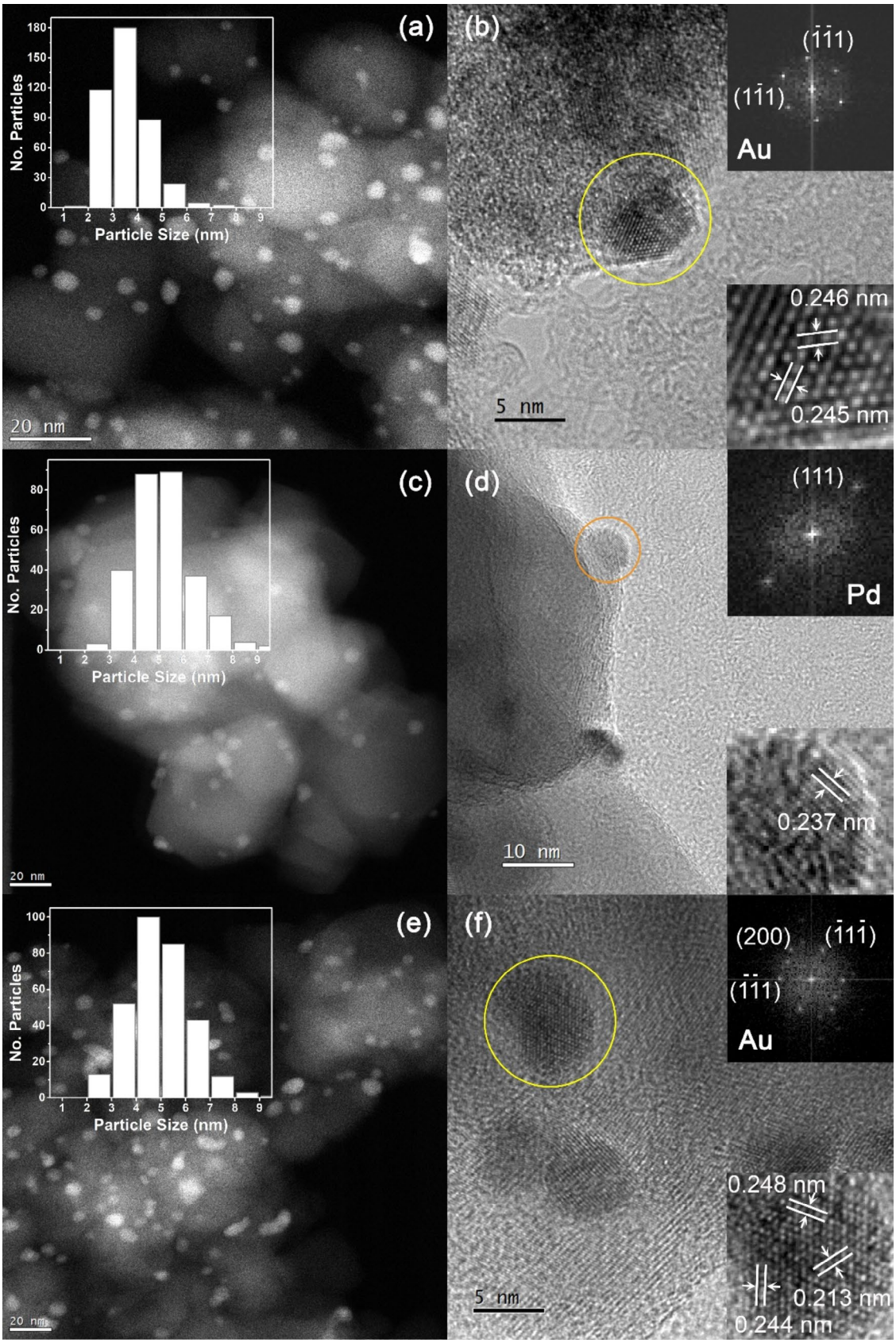

Fig. 6 Representative TEM images of the activated catalysts: (**a**) and (**b**) Au/TiO_2-D, (**c**) and (**d**) Pd/TiO_2-I, (**e**) and (**f**) AuPd/TiO_2-I_{Air}D. The particle size histogram is included in the HAADF images (**a**, **c** and **e**) while in (**b**, **d** and **f**) the HRTEM-FFT analysis of the lattice fringes is included

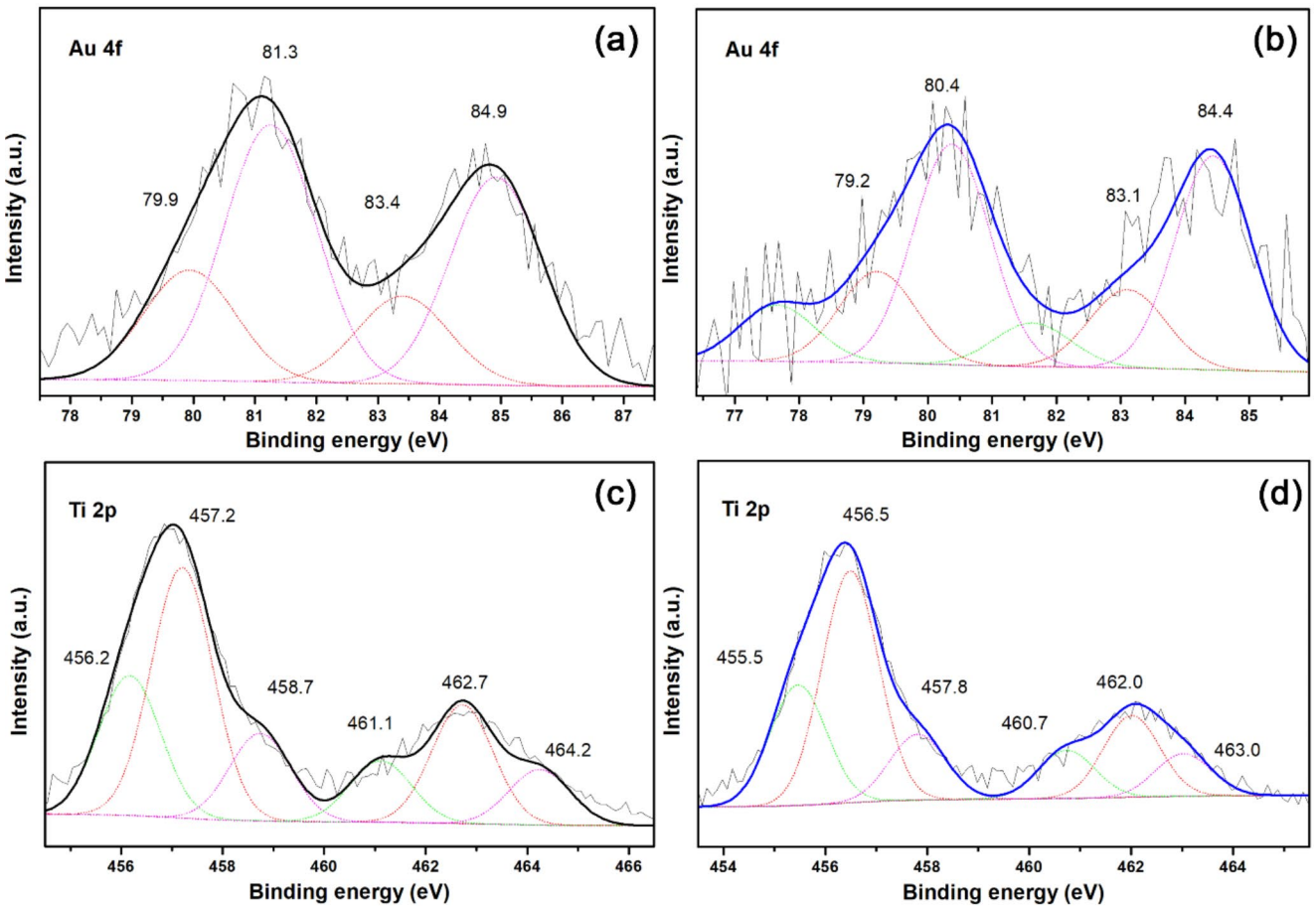

Fig. 7 X-ray photoelectron data of the activated catalysts: (**a** and **c**) the Au/TiO_2-D sample and (**b** and **d**) the AuPd/TiO_2-I_{Air}D sample. Spectra at different edges: (**a**, **b**) Au *4f* and (**c**, **d**) Ti *2p*

On the other hand, the Ti 2*p* edge deconvoluted spectra are presented in Fig. 7c, d. The doublet at around 457 eV (Ti $2p_{3/2}$) and 463 eV (Ti $2p_{1/2}$), and that located at around 458 eV (Ti $2p_{3/2}$) and 464 eV (Ti $2p_{1/2}$), were associated with Ti^{4+} species coming from the anatase and rutile phases, respectively. Moreover, the doublet at around 456 eV (Ti $2p_{3/2}$) and 461 eV (Ti $2p_{1/2}$) confirmed the generation of Ti^{3+} species in both catalysts [38]. The bimetallic AuPd/TiO_2-I_{Air}D sample exhibited two peculiarities in this region: (i) a shift towards lower binding energies, and (ii) an increase in the intensity ratio of the Ti^{3+} doublet. Both observations strongly suggested a larger presence of the partially reduced TiO_2 phase, in agreement with the XRD and Raman spectroscopy characterizations.

3.3 In-situ Characterization of Catalysts

3.3.1 Activation in H_2 Followed by in-situ UV-vis Spectroscopy

It has been well-established that gold and palladium metallic phases exhibit optical properties, specifically the surface plasmon resonance (SPR) phenomena [39, 40]. Therefore, to gain insights into the formation of the Au and Pd NPs in the monometallic samples, as well as in the Au-Pd interaction in the bimetallic catalyst, the activation process in a 10%H_2/Ar flow (60 mL min^{-1}) at 500 °C (2 °C min^{-1}) for 1 h was monitored through in-situ UV-vis diffuse reflectance spectroscopy, Fig. 8. Prior to the activation, the three samples presented strong absorption below 400 nm, the fingerprint of the optical response of the TiO_2 phase [41].

Figure 8a shows the spectra related to the Au/TiO_2-D sample. With the temperature increase (120 °C), a broad absorption band developed within the 750–400 nm interval, with absorption maxima (λ_{max}) at ca. 533 nm. At 140 °C, the absorption drastically increased, and, from this point,

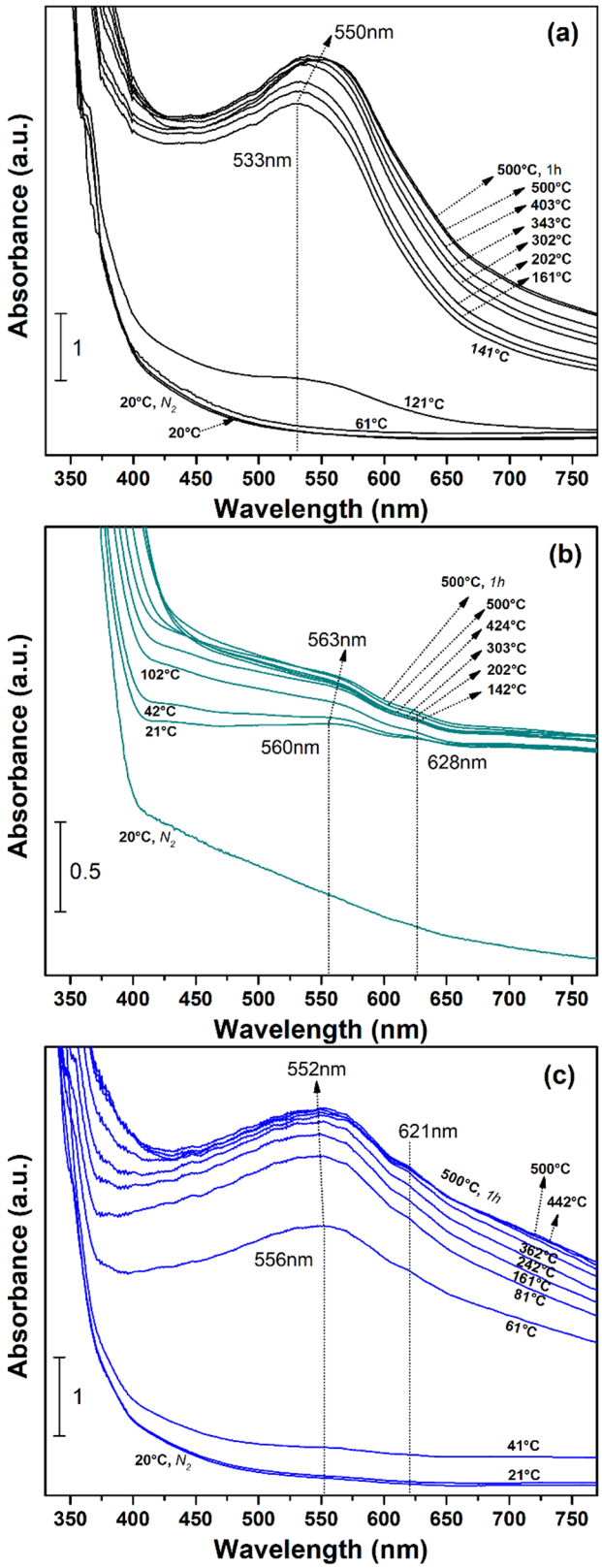

Fig. 8 Activation in H_2 (2 °C min^{-1}, 500 °C, 1 h) followed by in-situ UV-vis spectroscopy: (**a**) Au/TiO_2-D, (**b**) Pd/TiO_2-I, and (**c**) AuPd/TiO_2-I_{Air}D

this band slowly gained intensity until the final temperature (500 °C), with a final λ_{max} of 550 nm. According to the literature, this band is related to the localized surface plasmon resonance (LSPR) of metallic Au NPs (hereafter named as Au_{LSPR} band) [39, 42]. These results agreed with the H_2-TPR characterization, where the Au/TiO_2-D catalyst presented H_2 consumption at the 110–170 °C interval, almost the same temperature range where the Au_{LSPR} band was formed. Differences in the λ_{max} and intensity could be related to thermal effects, as reported previously [30, 43]. However, the reasons for these modifications could also be related to a slight increase in the size of the Au NPs [44].

Figure 8b presents the UV-vis spectra of the Pd/TiO_2-I sample. Immediately after admittance of the H_2 flow (20 °C), an abrupt increase in the absorption was observed, with two λ_{max} at 560 and 628 nm. Then, at the 40–500 °C interval, these contributions slightly increased in their absorption, with almost no shift in their λ_{max}. Results suggested that the LSPR band of the Pd NPs (hereafter named as Pd_{LSPR} band) was centered at 560 nm, in agreement with other reports [45]. This observation confirmed the H_2-TPR findings of the Pd/TiO_2-I sample, where it was proposed that the $Pd^{2+} \rightarrow Pd^0$ reduction occurred spontaneously at low temperatures. Moreover, based on the work by S. Mukherjee et al. [46], the contribution centered at 628 nm could also be assigned to the Pd_{LSPR} band arising from Pd NPs in strong interaction with the TiO_2 support. Regardless of the nature of this second band, results suggested a heterogeneity of the Pd species. Finally, compared to the gold catalyst, the intensity of the Pd_{LSPR} band decreased significantly; the above can be attributed to the damping effect caused by *d-d* inter-band transitions of palladium [47].

Figure 8c exhibits the spectra from the activation in H_2 of the AuPd/TiO_2-I_{Air}D sample. A broad absorption signal started developing at a relatively low temperature (40 °C), and suddenly increased at two steps: 40 and 60 °C. After this point, the signal slowly gained intensity until the final temperature (500 °C), and two λ_{max} at 552 and 621 nm were identified. The 552 nm contribution was located between the λ_{max} of both Au_{LSPR} and Pd_{LSPR} bands, suggesting that it originated from the LSPR of NPs composed of Au and Pd atoms in close interaction (hereafter named as $AuPd_{LSPR}$ band), in agreement with the HRTEM characterization. Besides, the observation of the 621 nm contribution suggests that the presence of palladium improved the interaction between the bimetallic NPs and the TiO_2 support. Finally, the temperature interval where the bimetallic AuPd/TiO_2-I_{Air}D catalyst exhibited hydrogen uptake in the H_2-TPR experiment (10–90 °C) almost matched with that observed when the LSPR band was completely developed, indicating that both support the formation of the bimetallic AuPd NPs.

3.3.2 CO Adsorption-Desorption Followed by In-situ DRIFTS

Carbon monoxide (CO), employed as a probe molecule, was adsorbed over the activated catalysts, to evidence the surface composition of mono and bimetallic NPs deposited over the TiO_2. CO adsorption was conducted at −20 °C to promote the formation of adsorbed carbonyls over the Au sites and to minimize the interference of the gas-phase molecules [48]. The evolution of the adsorbed carbonyl bands was monitored byin-situDRIFTS at two stages: (i) desorption at −20 °C in N_2 flow, and (ii) desorption upon heating (from −20 to 100 °C) in N_2 flow.

Figure 9a shows the FTIR spectra of the Au/TiO_2-D sample during the desorption step at −20 °C. At the beginning, three bands at 2170, 2112 and 2148 cm^{-1} were identified. At the end of this stage, only the last two remained visible. The 2170 cm^{-1} contribution was related either to the vibration of the gaseous CO [49], or to carbonyl species weakly adsorbed on Ti^{4+}/Ti^{3+} sites [50], thus explaining its disappearance after the purge. Linear carbonyl species adsorbed over low-coordinated metallic gold sites were responsible for the most intense 2112 cm^{-1} band (*l*CO-Au^0) [51], while linear carbonyls species adsorbed over negatively charged Au atoms accounted for the 2148 cm^{-1} band (*l*CO-$Au^{\delta-}$) [52]. The latter species were probably formed due to the strong interaction between the Au NPs and the TiO_2 support, promoting some electron transfer [53]. At the end of this stage, the *l*CO-Au^0 band slightly decreased. Moreover, at the heating stage in N_2 flow, Fig. 9b, the *l*CO-Au^0 band gradually decreased in intensity, while the *l*CO-$Au^{\delta-}$ band remained almost unaltered. However, at around 10 °C, both species completely disappeared, while an incipient contribution at 1995 cm^{-1} became visible; the latter probably linked to doubly-bridged carbonyls adsorbed on $Au^{\delta-}$ sites (*b*CO-$Au^{\delta-}$). Results confirmed the presence of well-dispersed metallic Au NPs in the activated Au/TiO_2-D catalyst, in agreement with the HRTEM and UV-vis results.

Figure 9c presents the FTIR spectra from the carbonyl region of the Pd/TiO_2-D catalyst during the CO desorption stage at −20 °C. Contributions at around 2094 and 2063 cm^{-1} were related to linear carbonyls adsorbed over metallic palladium sites (*l*CO-Pd^0), with high and low-coordination, respectively [54, 55]. Moreover, signals centered at ca. 1965 and 1923 cm^{-1} were attributed to doubly-bridged carbonyls adsorbed over Pd^0 sites (*b*CO-Pd^0) with high and low-coordination, respectively [56, 57]. Finally, the 1894 cm^{-1} band accounted for triply-bridged carbonyls over Pd^0 sites (*t*CO-Pd^0). The intensity of linear and bridged species was similar, with no modifications during this stage. However, all the contributions slowly decreased in intensity as the temperature increased, Fig. 9d. At 50 °C, linear species vanished and only remnants of the bridged species were observed, which agrees with their higher thermal stability previously reported [58]. Besides, compared to the spectra from the Au/TiO_2-D sample (Fig. 9b), a higher strength of the Pd sites towards adsorbed CO was evidenced. In summary, results verified that the activated Pd/TiO_2-I catalyst was composed of metallic Pd NPs deposited over the TiO_2 surface with different interaction (in agreement with the UV-vis characterization); likewise, the high population of bridged carbonyls could be linked to the existence of larger particle sizes, in agreement with the STEM characterization (see Table 1).

Figure 9e shows the spectra of the carbonyls desorption stage at −20 °C from the bimetallic AuPd/TiO_2-I_{Air}D catalyst. The analysis performed in the monometallic samples was considered to properly assign the nature of the observed vibrational bands. Four bands related linear carbonyls adsorbed over either gold or palladium sites were observed at around 2112 cm^{-1} (*l*CO-Au^0), 2081 cm^{-1} (*l*CO-Pd^0), 2069 cm^{-1} (*l*CO-Pd^0) and 2048 cm^{-1} (*l*CO-$Au^{\delta-}$). Besides, three bands associated with bridged carbonyls were identified at ca. 1959 cm^{-1} (*b*CO-Pd^0), 1948 cm^{-1} (*b*CO-Pd^0) and 1930 cm^{-1} (*t*CO-Pd^0). After 20 min of purge, the intensity of the *l*CO-Au^0 contribution marginally decreased, whereas those related to the Pd sites remained unaltered. Compared to the spectra of the monometallic Au/TiO_2-D (Fig. 9a) and Pd/TiO_2-I samples (Fig. 9c), three differences are worth mentioning: (i) the intensity of the carbonyl-on-Au bands decreased; (ii) all the carbonyl-on-Pd bands appeared shifted; and (iii) the population of the bridged species decreased, probably due to the presence of gold atoms on the nanoparticle surface, which hindered the formation of these species. All these observations suggested that the NPs present in the bimetallic AuPd/TiO_2-I_{Air}D catalyst were composed of an alloyed Au-Pd phase, with both atoms available on the surface.

Figure 9f presents the thermal stability of the above-mentioned bands coming from the AuPd/TiO_2-I_{Air}D catalyst. Both *l*CO-Au^0 and *l*CO-$Au^{\delta-}$ bands decreased with the temperature and totally disappeared at 5 °C, similar to the observed in the Au/TiO_2-D sample (Fig. 9b). Conversely, the thermal stability of the carbonyl-on-Pd bands increased, compared to that observed in the Pd/TiO_2-I sample (Fig. 9d). This modification was more important for the linear carbonyls, which remained visible up to 100 °C, specifically the *l*CO-Pd^0 band related to low-coordinated Pd atoms (2075 cm^{-1}). The improved stability of the carbonyls adsorbed over the Pd sites could be linked to the intimate interaction between Au and Pd atoms in the bimetallic NPs, and some electron transfer between the two elements, as evidenced in the Au*4f* edge spectrum of the bimetallic AuPd/TiO_2-I_{Air}D catalyst (see Fig. 7b).

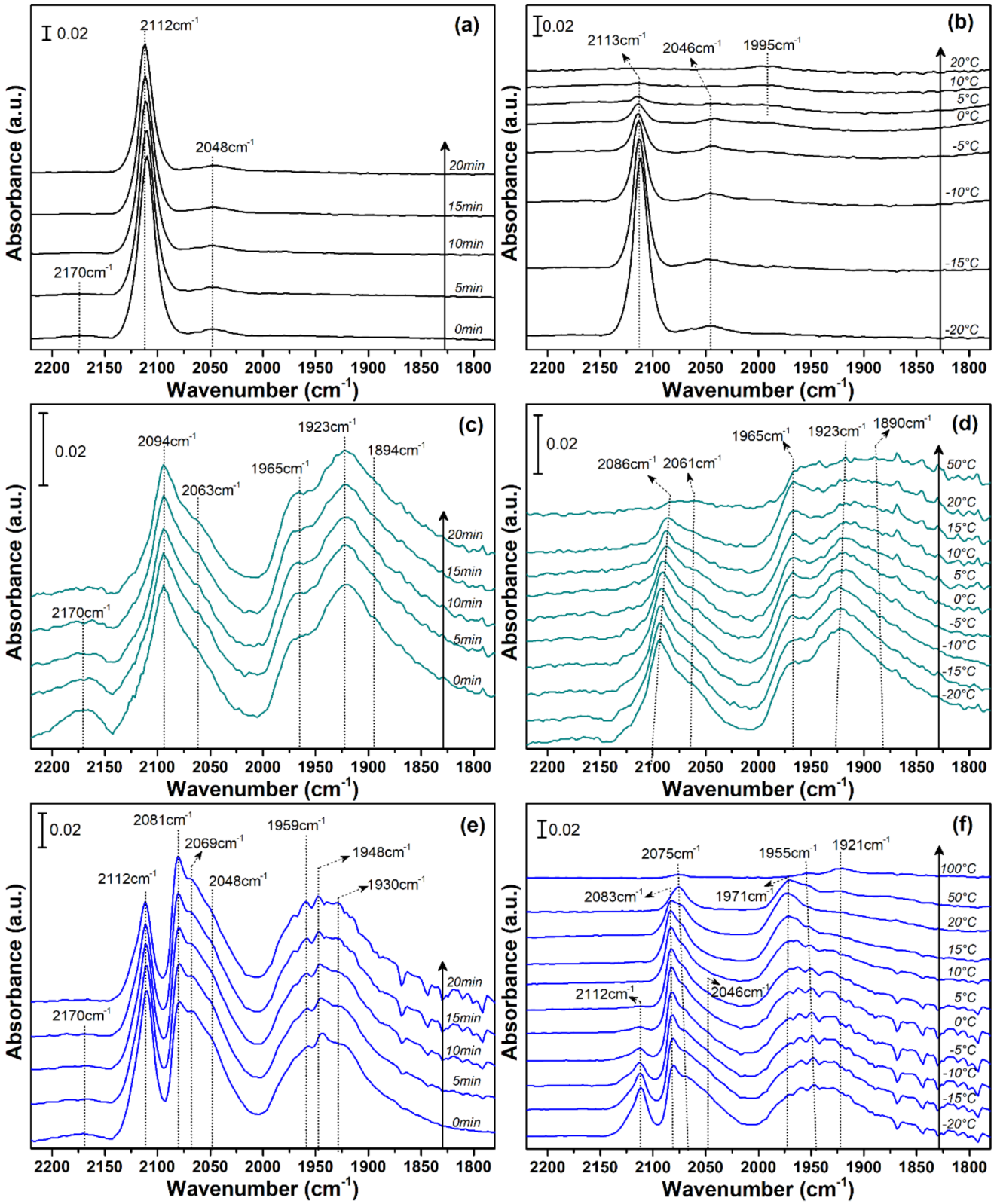

Fig. 9 CO adsorption-desorption followed by in-situ DRIFTS over activated catalysts: (**a**, **c**, and **e**) desorption at −20 °C in N_2 flow and (**b**, **d**, and **f**) desorption in N_2 flow upon heating. (a and b) the Au/TiO_2-D sample, (**c** and **d**) the Pd/TiO_2-I sample, and (e and f) the AuPd/TiO_2-I_{Air}D sample

3.4 CO Oxidation Studied via In-situ Spectroscopy Techniques

3.4.1 CO Oxidation Followed by In-situ DRIFT and UV-vis Spectroscopies

The behavior of the activated catalysts in the CO oxidation reaction (20–300 °C) was studied through in-situ spectroscopy techniques. Specifically, DRIFT (carbonyl region) and UV-vis (LSPR bands) spectroscopies were employed to determine the active sites and monitor the structural modifications that the supported NPs could experience in the reactive atmosphere. The discussion of the results was based mostly on the findings described in Sect. 3.3.1 and 3.3.2.

Figure 10a presents the FTIR spectra from the Au/TiO_2-D sample. Initially (20 °C), vibrations coming from gaseous CO (P and R branches), and linear carbonyls adsorbed on gold sites (*l*CO-Au^0 and *l*CO-$Au^{\delta-}$ bands) were observed. The nature of these contributions was unfolded in the previous section. Compared to the CO-adsorption-desorption experiment (see Fig. 8a, b), the intensity of the *l*CO-$Au^{\delta-}$ band decreased, suggesting that, in the reactive atmosphere ($CO+O_2$) the Au-TiO_2 interaction weakened. As the reaction temperature increased, the intensity of the carbonyl bands gradually decreased, and these completely disappeared at ca. 30 °C (*l*CO-Au^0) and ca. 150 °C (*l*CO-$Au^{\delta-}$). The disappearance of the *l*CO-$Au^{\delta-}$ band at low temperatures suggests that these sites (Au in strong interaction with the TiO_2 support) became less active as the temperature increased. At the same time, the intensity of the CO gas bands progressively diminished, however, these signals were still visible at the final temperature (300 °C).

Figure 10b shows the UV-vis absorption spectra of the Au/TiO_2-D catalyst during the CO oxidation reaction. After admittance of the reactive gases ($CO+O_2$), the λ_{max} of the Au_{LSPR} band shifted to lower wavelengths (compared to the spectrum of the activated catalyst shown in red). This shift was probably associated with the adsorption of carbonyl species over the Au NPs, which promoted some electron transfer from the molecule to the metal; a similar behavior was previously reported [30]. As the reaction temperature increased, the Au_{LSPR} band shifted to higher wavelengths, with a final λ_{max} of 546 nm at 300 °C (i.e., a 10 nm red-shift). This change was probably related to an increase in the Au NPs size [44]. In summary, both techniques helped to propose that the lower catalytic properties exhibited by Au/TiO_2-D sample (compared to the bimetallic one) could be related to the reduced activity of Au-TiO_2 sites, and the slight size increase of the Au NPs during the reaction.

Figure 10c shows the DRIFTS results coming from the Pd/TiO_2-I sample. Besides the gaseous CO, carbonyl bands adsorbed over Pd^0 linearly (*l*CO-Pd^0 at 2090 and 2063 cm^{-1}), doubly-bridged (*b*CO-Pd^0 at 1965 and 1930 cm^{-1}), and triply-bridged (*t*CO-Pd^0 at 1886 cm^{-1}) were observed at the first temperature (20 °C). Compared to the experiment in pure CO (see Fig. 8c, d), the intensity of the bridged carbonyls increased (especially the 1930 cm^{-1} contribution). This observation suggested that the size of the Pd NPs increased right from the beginning, a phenomenon probably promoted by the presence of O_2 in the reactive atmosphere by oxidizing some of the metallic Pd atoms to form PdOx. Upon heating, modifications in the position and intensity of the vibrational band were only noticed at 100 °C. The above suggests that below this temperature, the stability of the adsorbed carbonyls was too high, limiting their reactivity; this result agreed with the null activity exhibited by the Pd/TiO_2-I sample in this temperature interval (see Fig. 2a). The *l*CO-Pd^0 band related to high-coordinated Pd sites vanished at 200 °C, while the one related to low-coordinated Pd sites remained until the last temperature (300 °C). On the other hand, all three bridged carbonyls were still visible at the end of the experiment, however, the one related to the high-coordinated Pd sites (1965 cm^{-1}) presented a higher intensity at this stage. Remnants of CO gas were also observed at the final reaction temperature.

Figure 10d presents the UV-vis spectra of the Pd/TiO_2-I catalyst. The presence of the reactive atmosphere ($CO+O_2$) decreased the absorption intensity of the Pd_{LSPR} bands (with λ_{max} at 565 and 617 nm), and this behavior continued up to 100 °C. This phenomenon could be related to the oxidation of the Pd NPs in the presence of O_2, however, no carbonyl bands adsorbed on $Pd^{\delta+}$ were observed in the DRIFT spectra. Therefore, the decrease in absorption was probably related to the damping of the LSPR due to the high amount of carbonyl species adsorbed over the Pd NPs, as evidenced by DRIFTS (Fig. 10c). Above 100 °C, the Pd_{LSPR} bands gradually grew again, and, at the final temperature, these presented almost the same absorption intensity as that of the beginning. Interestingly, at the same temperature interval (100–300 °C), the intensity of adsorbed carbonyls decreased, a clear indication that both phenomena were linked. The λ_{max} of the Pd_{LSPR} bands remained unaltered during the complete reaction process. The combined DRIFTS and UV-vis in-situ characterization showed that the poor catalytic properties of the Pd/TiO_2-I catalyst were probably associated with the restructuring of the Pd NPs in the presence of the reactive atmosphere and the strong adsorption of the carbonyl species.

Figure 10e shows the CO oxidation in the activated AuPd/TiO_2-I_{Air}D sample, monitored by DRIFTS. At the beginning of the reaction (20 °C), carbonyl bands adsorbed linearly on Au^0 at 2110 cm^{-1} (*l*CO-Au^0) and over $Au^{\delta-}$ at 2046 cm^{-1} (*l*CO-$Au^{\delta-}$) were identified. Besides, carbonyl-on-Pd species adsorbed linearly (*l*CO-Pd^0 at 2079 and 2067 cm^{-1}),

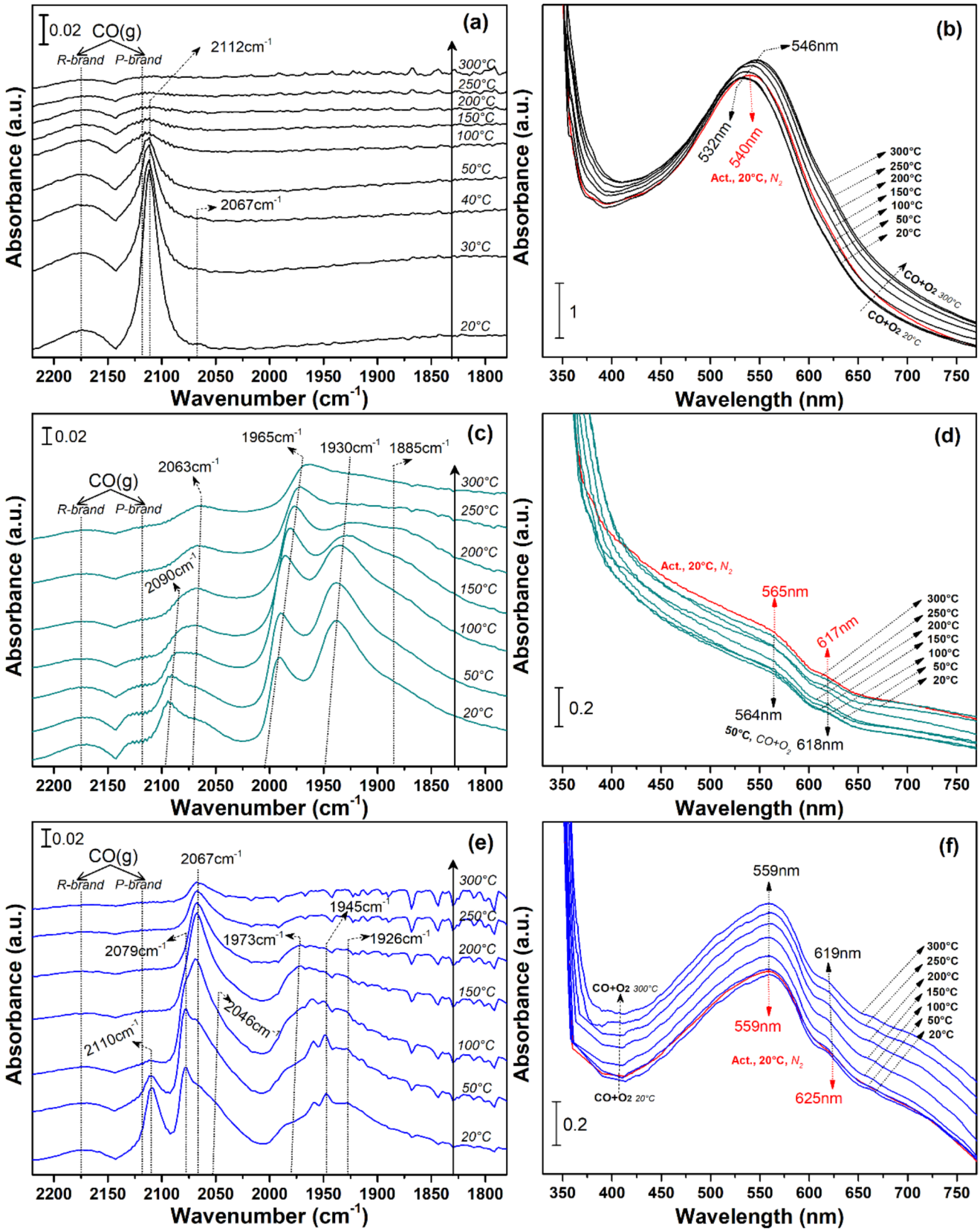

Fig. 10 CO oxidation followed by in-situ DRIFT (**a**, **c** and **e**) and in-situ UV-vis (b, d and f) spectroscopies over activated catalysts: (a and b) the Au/TiO_2-D sample and (**c** and **d**) the Pd/TiO_2-I sample, and (**e** and **f**) the AuPd/TiO_2-I_{Air}D sample

doubly-bridged (*b*CO-Pd^0 at 1973 and 1945 cm^{-1}), and triply-bridged (*t*CO-Pd^0 at 1926 cm^{-1}) were also observed at 20 °C. Except for the contribution of the CO gas, the profile was almost similar to the ones obtained in pure CO (see Fig. 8(e) and 8(d)), an indication that the O_2 did not affect the structure of the AuPd NPs. With the increase of the reaction temperature, both *l*CO-Au^0 and *l*CO-$Au^{\delta-}$ bands decreased and vanished above 100 °C. Compared to the Au/TiO_2-D catalyst (Fig. 10a), these contributions disappeared around the same temperature, however, the intensity of the *l*CO-$Au^{\delta-}$ band was higher in the bimetallic sample, suggesting that the Au-TiO_2 interaction increased by the presence of Pd, and these sites could be responsible for the higher activity at lower temperatures (see Fig. 2a). On the other hand, the analysis of carbonyls on Pd revealed that the linear species slowly decreased with increasing the temperature, while the carbonyls adsorbed on the low-coordinated Pd^0 sites (i.e., edges sites) remained visible at 300 °C. Although these contributions were also observed in the monometallic Pd/TiO_2-I sample (Fig. 10c), in the bimetallic one, they appeared blue-shifted, probably due to the close interaction with gold atoms and the electron transfer between the two, in agreement with the XPS characterization (see Fig. 7b). These low-coordinated Pd^0 atoms, in vicinity with the Au atoms, probably acted as additional active sites for the CO oxidation reaction at high temperatures. Finally, focusing on the bridged species, these disappeared at above 200 °C, while those observed in the monometallic palladium sample did not vanish at all. The above suggested that the presence of gold improved the adsorption strength of carbonyls-on-Pd to make them able to react. The absence of CO signals at high temperatures matched with the higher catalytic activity presented by this bimetallic sample (see Fig. 2(a)).

Figure 10f presents the UV-vis spectra of the AuPd/TiO_2-I_{Air}D catalyst during the CO oxidation reaction. Spectra of the activated bimetallic sample exhibited an absorption intensity between those of the monometallic counterparts, which reinforced the hypothesis of the formation of an intermetallic Au-Pd phase. After admittance of the reactive atmosphere at 20 °C ($CO+O_2$), only a slight decrease in the absorption of the $AuPd_{LSPR}$ band was observed (compared to the spectrum of the activated catalyst shown in red). This behavior diverged from the monometallic samples and indicated a higher stability of the bimetallic AuPd NPs. The absorption of the $AuPd_{LSPR}$ band increased with the reaction temperature, however the λ_{max} at 559 nm remained unaltered. These two observations suggested that the increased absorption was associated with a thermal effect rather than with the sintering of the AuPd NPs. On the other hand, the second contribution blue-shifted from 625 to 619 nm. As proposed in Sect. 3.3.1, this band may arise from bimetallic AuPd NPs in close interaction with the TiO_2 support, therefore, the shift may suggest a modification of this interplay during the reaction. Since DRIFTS results did not evidence modifications of the bimetallic NPs, this phenomenon could be related to changes in TiO_2 support. In the following section, this proposal is discussed in detail.

Overall, the in-situ monitoring of the CO oxidation reaction in the AuPd/TiO_2-I_{Air}D catalyst led to the following proposals: (i) the bimetallic AuPd NPs maintain a stable structure during the reaction; (ii) at low temperatures, Au atoms in close interaction with the TiO_2 support served as the active sites, while at high temperatures, low-coordinated Pd atoms were likely the active sites; and (iii) Au enhanced the reactivity of Pd, and vice versa.

3.4.2 CO Oxidation Followed by In-situ Raman Spectroscopy

The role of the TiO_2 support during the CO oxidation reaction (20–300 °C) was unveiled through in-situ Raman spectroscopy. The analysis considered the results described in Sect. 3.2.1.

Figure 11a presents the normalized Raman spectra of the activated bimetallic AuPd/TiO_2-I_{Air}D catalyst exposed to the reactive atmosphere. All the previously described Raman active modes, related to the TiO_2 anatase phase (Sect. 3.2.1), were also identified in these experiments. Focusing on the $E_{g(1)}$ mode, sensitive to the formation of oxygen vacancies (Vö) and the partial reduction of the TiO_2 phase [29], a continuous blueshift was evidenced with the reaction temperature increase (see inset Fig. 11a). The $E_{g(1)}$ band maximum ended at 153.0 cm^{-1}, i.e., a total shift of 8.7 cm^{-1} (compared to the position of the dried sample). The temperature dependency on the shift of the TiO_2 Raman bands has been studied and reported to be below 5 cm^{-1} [59, 60], nevertheless, the displacement of the AuPd/TiO_2-I_{Air}D catalyst in the present work was more important. Therefore, this result revealed that a partial TiO_2 reduction during the CO oxidation reaction took place in the bimetallic sample. This process could be ascribed to the presence of CO in the reactive atmosphere, a molecule known for being a reductive agent [61]. Therefore, the better catalytic properties of the bimetallic sample (see Fig. 2) resulted also from the partial reduction of the TiO_2 support, as the Vö sites could be also active in the CO oxidation reaction [62]. Additionally, these oxygen vacancies may account for the lower E_a value of the AuPd/TiO_2-I_{Air}D sample (see Table 3), which is consistent with previous reports [63].

To clarify the impact of the bimetallic AuPd NPs on the partial reduction of the TiO_2, the activation in H_2 and the CO oxidation reaction were monitored in both the bare TiO_2 support and the bimetallic AuPd/TiO_2-I_{Air}D catalyst, Figs. S4 and S5, correspondingly. Figure 11b summarizes

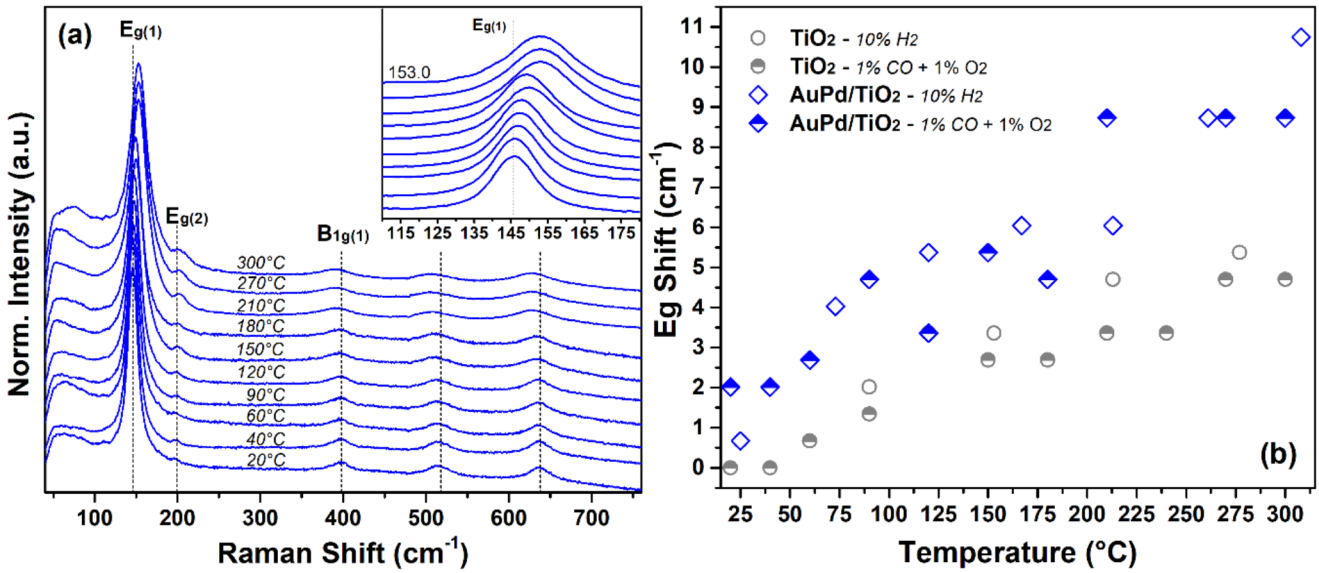

Fig. 11 (**a**) Normalized Raman spectra of the activated AuPd/TiO_2-I_{Air}D catalyst during the CO oxidation reaction (20–300 °C). (**b**) Main TiO_2 anatase Raman peak ($Eg_{(1)}$) shifts (relative to the position in bare TiO_2 at 20 °C) as a function of the temperature at different flowing atmospheres (10%H_2 and 1%CO + 1%O_2) over the TiO_2 and AuPd/TiO_2-I_{Air}D samples

the above-mentioned in-situ Raman measurements, the plot correlated the $Eg_{(1)}$ mode shifts (relative to the observed in bare TiO_2 at 20 °C (ca. 144 cm^{-1})) vs. the temperature of the process. Results indicated that the blueshift of the $E_{g(1)}$ mode was more important in the AuPd/TiO_2-I_{Air}D sample. Furthermore, this shift was larger in the H_2 atmosphere, a somehow expected result considering that hydrogen is the best reductive agent. Conversely, the displacement observed in the bare TiO_2 support was lower than 5 cm^{-1}, regardless of the atmosphere, and probably associated only with thermal effects. Overall, results strongly suggested that, under reaction conditions (CO + O_2), the partial TiO_2 reduction was promoted by the presence of bimetallic AuPd NPs interacting closely with the support. This partial TiO_2 restructuration was proposed to be included as part of the reasons why the bimetallic AuPd/TiO_2-I_{Air}D catalyst presented the best catalytic properties in the CO oxidation reaction.

4 Conclusions

Bimetallic AuPd/TiO_2 catalysts, with a targeted Au: Pd atomic ratio of 1, were successfully prepared through a sequential impregnation (Pd) and deposition-precipitation in urea (Au) methodology over a commercial TiO_2 support. An intermediate thermal treatment in an air atmosphere, between the Pd and the Au addition, boosted the catalytic activity and stability of the bimetallic AuPd/TiO2-I_{Air}D sample. The CO conversion at 0 °C was almost five times larger in the bimetallic catalyst, compared to the gold monometallic one.

Ex-situ characterization (XRD, Raman spectroscopy, H_2-TPR, HRTEM and XPS spectroscopy) revealed the key features that boosted the catalytic properties of the bimetallic AuPd/TiO2-I_{Air}D sample: (i) strong gold-palladium interaction and (ii) enhanced TiO_2 reducibility promoted by the presence of both Au and Pd species. The monitoring of the activation in H_2 (UV-vis) and CO-adsorption at −20 °C (DRIFTS) processes indirectly corroborated that the NPs in the bimetallic AuPd/TiO2-I_{Air}D sample were composed of an intermetallic alloy with both Au and Pd atoms at the surface.

The study of the CO oxidation reaction through the combination of in-situ DRIFT, UV-vis and Raman spectroscopies was helpful on proposing the different active sites of the AuPd/TiO2-I_{Air}D catalyst: (i) Au atoms in close interaction with the TiO_2 support, (ii) low-coordinated Pd atoms interacting closely with gold, and (iii) Vö sites from the partially reduced TiO_2 support.

Supplementary Information The online version contains supplementary material available at https://doi.org/10.1007/s11244-025-02051-w.

Acknowledgements The present work was financially supported by DGAPA-PAPIIT (104022) and CONAHCYT (A1-S-18269) projects. Authors acknowledge the *Laboratorio Universitario de Caracterización Espectroscópica* (LUCE-ICAT), Selene R. Islas and Roberto Y. Sato-Berrú, for the help provided in the characterization of materials. Finally, D. G. Araiza acknowledges DGAPA-UNAM for the granted postdoctoral scholarship.

Author Contributions Conceptualization: D. G. Araiza, R. Zanella; Methodology: D.G. Araiza, V. Maturano-Rojas; Validation: D.G. Araiza, M. Fernández, M. Sánchez-Ugalde; Formal analysis: D.G. Araiza,

M. Fernández, M. Sánchez-Ugalde, A. Miranda, D.A. Solís-Casados; Investigation: D.G. Araiza, M. Fernández, M. Sánchez-Ugalde, A. Miranda, D.A. Solís-Casados, V. Maturano-Rojas; Resources: R. Zanella; Data Curation: D.G. Araiza, M. Fernández, M. Sánchez-Ugalde; Writing - Original Draft: D.G. Araiza, R. Zanella; Writing - Review & Editing: D.G. Araiza, V. Maturano-Rojas, R. Zanella. Visualization: D.G. Araiza, M. Fernández; Supervision: R. Zanella; Project administration: D.G. Araiza, V. Maturano-Rojas; Funding acquisition: R. Zanella.

References

1. Panayotov DA, Morris JR (2016) Surface chemistry of Au/TiO2: thermally and photolytically activated reactions. Surf Sci Rep 71:77–271. https://doi.org/10.1016/j.surfrep.2016.01.002
2. Spezzati G, Benavidez AD, DeLaRiva AT et al (2019) CO oxidation by pd supported on CeO2(100) and CeO2(111) facets. Appl Catal B 243:36–46. https://doi.org/10.1016/j.apcatb.2018.10.015
3. Epling WS, Hoflund GB, Weaver JF et al (1996) Surface characterization study of au / α-Fe $_2$ O $_3$ and Au/Co $_3$ O $_4$ low-temperature CO oxidation catalysts. J Phys Chem 100:9929–9934. https://doi.org/10.1021/jp960593t
4. Haruta M (2003) When gold is not noble: catalysis by Nanoparticles. Chem Record 3:75–87. https://doi.org/10.1002/tcr.10053
5. Huaqing Z, Zhangfeng Q, Wenjuan S et al (2004) Pd/CeO2-TiO2 catalyst for CO oxidation at low temperature: a TPR study with H2 and CO as reducing agents. J Catal 225:267–277. https://doi.org/10.1016/j.jcat.2004.04.006
6. Delannoy L, Giorgio S, Mattei JG et al (2013) Surface segregation of pd from TiO $_2$ -Supported AuPd nanoalloys under CO oxidation conditions observed in situ by ETEM and DRIFTS. ChemCatChem 5:2707–2716. https://doi.org/10.1002/cctc.201200618
7. Beck A, Horváth A, Schay Z et al (2007) Sol derived gold–palladium bimetallic nanoparticles on TiO2: structure and catalytic activity in CO oxidation. Top Catal 44:115–121. https://doi.org/10.1007/s11244-007-0284-x
8. Tofighi G, Yu X, Lichtenberg H et al (2019) Chemical Nature of Microfluidically Synthesized AuPd Nanoalloys supported on TiO $_2$. ACS Catal 9:5462–5473. https://doi.org/10.1021/acscatal.9b00161
9. Guczi L (2003) AuPd bimetallic nanoparticles on TiO2: XRD, TEM, in situ EXAFS studies and catalytic activity in CO oxidation. J Mol Catal Chem 204–205:545–552. https://doi.org/10.1016/S1381-1169(03)00337-6
10. Betti C, Badano J, Maccarrone MJ et al (2012) Effect of the sequence of impregnation on the activity and sulfur resistance of Pt–Ni/γ-Al2O3 bimetallic catalysts for the selective hydrogenation of styrene. Appl Catal Gen 435–436:181–186. https://doi.org/10.1016/j.apcata.2012.06.001
11. Shimura K, Miyazawa T, Hanaoka T, Hirata S (2015) Fischer-Tropsch synthesis over alumina supported bimetallic co-ni catalyst: Effect of impregnation sequence and solution. J Mol Catal Chem 407:15–24. https://doi.org/10.1016/j.molcata.2015.06.013
12. Díaz G, Gómez-Cortés A, Hernández-Cristobal O et al (2011) Hydrogenation of Citral over IrAu/TiO2 catalysts. Effect of the Preparation Method. Top Catal 54:467–473. https://doi.org/10.1007/s11244-011-9609-x
13. Sandoval A, Aguilar A, Louis C et al (2011) Bimetallic Au–Ag/TiO2 catalyst prepared by deposition–precipitation: high activity and stability in CO oxidation. J Catal 281:40–49. https://doi.org/10.1016/j.jcat.2011.04.003
14. Camposeco R, Hinojosa-Reyes M, Castillo S et al (2021) Synthesis and characterization of highly dispersed bimetallic Au-Rh nanoparticles supported on titanate nanotubes for CO oxidation reaction at low temperature. Environ Sci Pollut Res 28:10734–10748. https://doi.org/10.1007/s11356-020-11341-7
15. Calzada LA, Louis C, Wan Han C et al (2020) Au-Ru/TiO2 prepared by deposition-precipitation with urea: relevant synthesis parameters to obtain bimetallic particles. Appl Catal B 264:118503. https://doi.org/10.1016/j.apcatb.2019.118503
16. Meunier FC (2016) Pitfalls and benefits of in situ and operando diffuse reflectance FT-IR spectroscopy (DRIFTS) applied to catalytic reactions. React Chem Eng 1:134–141. https://doi.org/10.1039/C5RE00018A
17. Hunger M, Weitkamp J (2001) In situ IR, NMR, EPR, and UV/Vis spectroscopy: tools for New Insight into the mechanisms of Heterogeneous Catalysis. Angew Chem Int Ed 40:2954–2971
18. Li X, Blinn K, Chen D, Liu M (2018) In situ and surface-enhanced Raman Spectroscopy Study of Electrode materials in solid oxide fuel cells. Electrochem Energy Reviews 1:433–459. https://doi.org/10.1007/s41918-018-0017-9
19. Araiza DG, Gómez-Cortés A, Díaz G (2020) Methanol decomposition over bimetallic Cu-M catalysts supported on nanoceria: Effect of the second metal on the catalytic properties. Catal Today 356:440–455. https://doi.org/10.1016/j.cattod.2019.04.076
20. Wang X, Rosspeintner A, Ziarati A et al (2022) Insight into the transient inactivation effect on Au/TiO2 catalyst by in-situ DRIFT and UV–vis spectroscopy. Nat Commun 13:5458. https://doi.org/10.1038/s41467-022-33187-y
21. Lee Y, He G, Akey AJ et al (2011) Raman Analysis of Mode Softening in Nanoparticle CeO $_{2-\delta}$ and Au-CeO $_{2-\delta}$ during CO oxidation. J Am Chem Soc 133:12952–12955. https://doi.org/10.1021/ja204479j
22. Sandoval A, Louis C, Zanella R (2013) Improved activity and stability in CO oxidation of bimetallic Au–Cu/TiO2 catalysts prepared by deposition–precipitation with urea. Appl Catal B 140–141:363–377. https://doi.org/10.1016/j.apcatb.2013.04.039
23. Toby BH, Von Dreele RB (2013) *GSAS-II*: the genesis of a modern open-source all purpose crystallography software package. J Appl Crystallogr 46:544–549. https://doi.org/10.1107/S0021889813003531
24. Prati L, Villa A, Porta F et al (2007) Single-phase gold/palladium catalyst: the nature of synergistic effect. Catal Today 122:386–390. https://doi.org/10.1016/j.cattod.2006.11.003
25. Díaz-Carrasco P, Kuhn A, Menéndez N, García-Alvarado F (2023) Reversible Fe3+/Fe2+and Ti4+/Ti3+redox couple in Fe-substituted LiTi2O4 ramsdellite and its electrochemical properties as electrode material in lithium ion batteries. J Alloys Compd 968:172027. https://doi.org/10.1016/j.jallcom.2023.172027
26. Shannon RD (1976) Revised effective ionic radii and systematic studies of interatomic distances in halides and chalcogenides. Acta Crystallogr Sect A 32:751–767. https://doi.org/10.1107/S0567739476001551
27. Martínez Tejada LM, Muñoz A, Centeno MA, Odriozola JA (2016) *In-situ* Raman spectroscopy study of Ru/TiO $_2$ catalyst in the selective methanation of CO. J Raman Spectrosc 47:189–197. https://doi.org/10.1002/jrs.4774

28. Yang C-H, Ma Z-Q (2012) Raman spectral analysis of TiO_2 thin films doped with rare-earth samarium. Appl Opt 51:5438. https://doi.org/10.1364/AO.51.005438
29. Parker JC, Siegel RW (1990) Calibration of the Raman spectrum to the oxygen stoichiometry of nanophase TiO2. Appl Phys Lett 57:943–945. https://doi.org/10.1063/1.104274
30. Araiza DG, Celaya CA, Solís-Casados DA et al (2024) Unveiling the structural behavior of bimetallic AuCu/TiO2 catalysts in the CO oxidation: a combined in-situ spectroscopic and theoretical study. Chem Eng J 494:152921. https://doi.org/10.1016/j.cej.2024.152921
31. Wei S, Fu X-P, Wang W-W et al (2018) Au/TiO_2 catalysts for CO Oxidation: Effect of Gold State to Reactivity. J Phys Chem C 122:4928–4936. https://doi.org/10.1021/acs.jpcc.7b12418
32. Idakiev V, Tabakova T, Yuan Z-Y, Su B-L (2004) Gold catalysts supported on mesoporous titania for low-temperature water–gas shift reaction. Appl Catal Gen 270:135–141. https://doi.org/10.1016/j.apcata.2004.04.030
33. Gluhoi AC, Tang X, Marginean P, Nieuwenhuys BE (2006) Characterization and catalytic activity of unpromoted and alkali (earth)-promoted Au/Al2O3 catalysts for low-temperature CO oxidation. Top Catal 39:101–110. https://doi.org/10.1007/s11244-006-0043-4
34. Zhang C, Li Y, Wang Y, He H (2014) Sodium-promoted Pd/TiO_2 for Catalytic Oxidation of Formaldehyde at Ambient temperature. Environ Sci Technol 48:5816–5822. https://doi.org/10.1021/es4056627
35. Cárdenas-Lizana F, Gómez-Quero S, Keane MA (2008) Ultra-selective gas phase catalytic hydrogenation of aromatic nitro compounds over Au/Al2O3. Catal Commun 9:475–481. https://doi.org/10.1016/j.catcom.2007.07.032
36. Escobar J, Colín-Luna JA, Barrera MC (2024) Thioresistant PdPt/Al/SBA-15 for Naphthalene Hydrogenation. Ind Eng Chem Res 63:1248–1260. https://doi.org/10.1021/acs.iecr.3c02359
37. Sahoo SR, Ke S-C (2021) Spin-Orbit Coupling effects in au 4f core-level electronic structures in supported low-dimensional gold nanoparticles. Nanomaterials 11:554. https://doi.org/10.3390/nano11020554
38. Camposeco R, Zanella R (2022) Multifunctional Pt-Cu/TiO2 nanostructures and their performance in oxidation of soot, formaldehyde, and carbon monoxide reactions. Catal Today 392–393:23–30. https://doi.org/10.1016/j.cattod.2021.06.025
39. Eustis S, El-Sayed MA (2006) Why gold nanoparticles are more precious than pretty gold: noble metal surface plasmon resonance and its enhancement of the radiative and nonradiative properties of nanocrystals of different shapes. Chem Soc Rev 35:209–217. https://doi.org/10.1039/B514191E
40. Chang X, Wang Y-F, Zhang X et al (2019) Enhanced ultraviolet absorption in diamond surface via localized surface plasmon resonance in palladium nanoparticles. Appl Surf Sci 464:455–457. https://doi.org/10.1016/j.apsusc.2018.09.087
41. Lin Z, Wang X, Liu J et al (2015) On the role of localized surface plasmon resonance in UV-Vis light irradiated Au/TiO_2 photocatalysis systems: pros and cons. Nanoscale 7:4114–4123. https://doi.org/10.1039/C4NR06929C
42. Seh ZW, Liu S, Low M et al (2012) Janus Au-TiO_2 photocatalysts with strong localization of Plasmonic Near-Fields for efficient visible-light hydrogen generation. Adv Mater 24:2310–2314. https://doi.org/10.1002/adma.201104241
43. Mancilla A, Mendoza-Cruz R, Portales B, Zanella R (2024) Catalytic oxidation of carbon monoxide at low temperature using AuRh/TiO2 bimetallic catalysts: Effect of the synthesis method. Mater Today Chem. https://doi.org/10.1016/j.mtchem.2024.102092
44. Cárdenas-Lizana F, Gómez-Quero S, Idriss H, Keane MA (2009) Gold particle size effects in the gas-phase hydrogenation of m-dinitrobenzene over Au/TiO2. J Catal 268:223–234. https://doi.org/10.1016/j.jcat.2009.09.020
45. Lacerda AM, Larrosa I, Dunn S (2015) Plasmon enhanced visible light photocatalysis for TiO_2 supported pd nanoparticles. Nanoscale 7:12331–12335. https://doi.org/10.1039/C5NR03659C
46. Mukherjee S, Libisch F, Large N et al (2013) Hot electrons do the impossible: Plasmon-Induced dissociation of H_2 on au. Nano Lett 13:240–247. https://doi.org/10.1021/nl303940z
47. Al-Azri ZHN, Chen W-T, Chan A et al (2015) The roles of metal co-catalysts and reaction media in photocatalytic hydrogen production: performance evaluation of M/TiO2 photocatalysts (M = pd, pt, au) in different alcohol–water mixtures. J Catal 329:355–367. https://doi.org/10.1016/j.jcat.2015.06.005
48. Li D, Chen S, You R et al (2018) Titania-morphology-dependent dual-perimeter-sites catalysis by Au/TiO2 catalysts in low-temperature CO oxidation. J Catal 368:163–171. https://doi.org/10.1016/j.jcat.2018.09.032
49. Bak J, Clausen S (1999) Signal-to-Noise Ratio of FT-IR CO Gas Spectra. Appl Spectrosc. https://doi.org/10.1366/0003702991947135
50. Hadjiivanov KI, Vayssilov GN (2002) Characterization of oxide surfaces and zeolites by carbon monoxide as an IR probe molecule. pp 307–511
51. Mihaylov M, Knözinger H, Hadjiivanov K, Gates BC (2007) Characterization of the Oxidation States of supported gold species by IR Spectroscopy of Adsorbed CO. Chem Ing Tech 79:795–806. https://doi.org/10.1002/cite.200700029
52. Chakarova K, Mihaylov M, Ivanova S et al (2011) Well-defined negatively charged gold carbonyls on Au/SiO_2. J Phys Chem C 115:21273–21282. https://doi.org/10.1021/jp2070562
53. Vindigni F, Manzoli M, Chiorino A, Boccuzzi F (2009) Catalytically active gold sites: nanoparticles, borderline sites, clusters, cations, anions? FTIR spectra analysis of12CO and of12CO-13CO isotopic mixtures. Gold Bull 42:106–112. https://doi.org/10.1007/BF03214920
54. Lear T, Marshall R, Antonio Lopez-Sanchez J et al (2005) The application of infrared spectroscopy to probe the surface morphology of alumina-supported palladium catalysts. J Chem Phys. https://doi.org/10.1063/1.2101487
55. Chen J, Wu Y, Hu W et al (2020) New insights into the role of Pd-Ce interface for methane activation on monolithic supported pd catalysts: a step forward the development of novel PGM three-way catalysts for natural gas fueled engines. Appl Catal B 264:118475. https://doi.org/10.1016/j.apcatb.2019.118475
56. Murata K, Mahara Y, Ohyama J et al (2017) The metal–support Interaction concerning the particle size effect of Pd/Al 2 O 3 on methane Combustion. Angew Chem 129:16209–16213. https://doi.org/10.1002/ange.201709124
57. Zorn K, Giorgio S, Halwax E et al (2011) CO oxidation on technological Pd-Al2O3 catalysts: oxidation state and activity. J Phys Chem C 115:1103–1111. https://doi.org/10.1021/jp106235x
58. Bourguignon B, Carrez S, Dragnea B, Dubost H (1998) Vibrational spectroscopy of imperfect CO/Pd(111) surfaces obtained by adsorption between 150 and 230K. Surf Sci 418:171–180. https://doi.org/10.1016/S0039-6028(98)00714-6
59. Shirpay A, Tavakoli M (2022) The behavior of the active modes of the anatase phase of TiO2 at high temperatures by Raman scattering spectroscopy. Indian J Phys 96:1673–1681. https://doi.org/10.1007/s12648-021-02123-z
60. Du YL, Deng Y, Zhang MS (2006) Variable-temperature Raman scattering study on anatase titanium dioxide nanocrystals. J Phys Chem Solids 67:2405–2408. https://doi.org/10.1016/j.jpcs.2006.06.020
61. Zhu H, Qin Z, Shan W et al (2004) Pd/CeO2-TiO2 catalyst for CO oxidation at low temperature: a TPR study with H2 and CO

as reducing agents. J Catal 225:267–277. https://doi.org/10.1016/j.jcat.2004.04.006
62. Chen W, Xu J, Huang F et al (2023) CO oxidation over CuOx/TiO2 catalyst: the importance of oxygen vacancies and cu+ species. Appl Surf Sci 618:156539. https://doi.org/10.1016/j.apsusc.2023.156539
63. Camposeco R, Torres AE, Zanella R (2022) Influence of the Preparation method of au, pd, pt, and Rh/TiO2 nanostructures and their Catalytic activity on the CO oxidation at low temperature. Top Catal 65:798–816. https://doi.org/10.1007/s11244-022-01607-4